Dalton Transactions

In situ Raman investigation of Dy complexation in Cl-bearing aqueous solutions at 20-300 °C

Journal:	*Dalton Transactions*
Manuscript ID	DT-ART-07-2024-002170.R2
Article Type:	Paper
Date Submitted by the Author:	23-Jan-2025
Complete List of Authors:	Smith-Schmitz, Sarah; New Mexico Bureau of Geology & Mineral Resources, New Mexico Institute of Mining and Technology Hurtig, Nicole; New Mexico Institute of Mining and Technology, Earth and Environmental Science; New Mexico Tech Gysi, Alexander; New Mexico Institute of Mining and Technology, Earth and Environmental Science; New Mexico Bureau of Geology & Mineral Resources, New Mexico Institute of Mining and Technology

In situ Raman investigation of Dy complexation in Cl-bearing aqueous solutions at 20-300 °C

Sarah E. Smith-Schmitz[1*], Nicole C. Hurtig[2], Alexander P. Gysi[1]

[1] New Mexico Bureau of Geology and Mineral Resources, New Mexico Institute of Mining and Technology, 801 Leroy Place, 87801 Socorro
[2] Dept. of Earth and Environmental Sciences, New Mexico Institute of Mining and Technology, 801 Leroy Place, 87801 Socorro
*corresponding author: sarah.smith@nmt.edu

Keywords: Dy speciation, Raman spectroscopy, hydrothermal fluids

Abstract

Raman spectroscopy provides a versatile tool for *in situ* characterization of aqueous rare earth elements (REE) speciation at the molecular level. Complexation of REE with ligands such as Cl^- and OH^- is of particular interest for understanding the mobility of REE in NaCl-bearing hydrothermal fluids responsible for enriching REE to economic levels in nature. Raman spectroscopic studies of REE speciation in Cl-bearing aqueous fluids are primarily conducted at ambient temperature, whereas natural systems indicate temperatures of >100–600 °C. In this study, the speciation of Dy in acidic chloride-bearing hydrothermal solutions was investigated using confocal Raman spectroscopy equipped with a new capillary Raman heating stage at 20–300 °C. Background solutions (pure water, NaCl-solutions) and solutions with 0.14–1.8 mol/kg dissolved $DyCl_3$ were sealed in quartz capillary cells. Comparison of the spectra for Dy chloride solutions with those for background solutions and the spectra for reference Dy-bearing solids was used to identify Raman bands specific to Dy-O and Dy-Cl bonds. The Raman band for the Dy-O stretching mode of hydrated Dy^{3+} aqua ions was measured at 365–384 cm^{-1} and a Raman band for the Dy-Cl stretching modes of Dy chloride complexes was measured near 240 cm^{-1}. The Dy-O band decreases systematically with temperature, whereas the Dy-Cl band systematically increases, indicating a systematic increase in the stability of Dy chloride complexes with temperature. This study provides the framework for expanding the use of *in situ* Raman spectroscopy to investigate the speciation of REE in aqueous solutions to hydrothermal conditions.

Introduction

The rare earth elements (REE) are composed of the 15 lanthanides (La-Lu) plus Y and Sc [1] and can be further subdivided into light (L)REE, comprising La-Gd, and heavy (H)REE, consisting of Tb-Lu and Y. The LREE/HREE are commonly grouped based on their chemical properties such as their increasing atomic mass and decreasing ionic radius from LREE to HREE [1]. Dysprosium (Dy) is primarily used to improve the temperature stability and performance of NdFeB permanent magnets used in offshore wind turbines and electric vehicles [2–5]. Due to the importance of Dy to sustainable energy technologies it is included in the recent United States Department of Energy Critical Materials List [6]. In natural geologic systems, hydrothermal fluids play a key role in the enrichment of REE mineral deposits, which form due to a combination of magmatic and hydrothermal processes [7–9]. In NaCl-bearing hydrothermal fluids at acidic conditions, geochemical simulations predict REE chloride complexes to be the most important species whereas the REE^{3+} species dominate at low temperature [7,10].

Geochemical simulations depend on accurate measurement of thermodynamic properties for REE complexes at relevant temperature and pressure, which are based on experimental studies, including solubility experiments [11,12], UV-vis speciation experiments [13–16], time resolved laser-induced spectroscopy [17,18], *in situ* Raman spectroscopy [19–24], and X-ray absorption spectroscopy experiments (XAFS) [25–31]. Experimental studies of the speciation of the REE in chloride-bearing solutions indicate that the REE^{3+} aqua ion is the dominant REE species at ambient temperature and low pH, and that $REECl^{2+}$ and $REECl_2^{+}$ are the primary REE chloride complexes to form at temperatures above 200 to 300 °C [7,30–33]. The stability of REE chloride complexes increases with temperature with the LREE over the HREE in hydrothermal fluids

[7,30,31]. X-ray absorption spectroscopy experiments show that REE^{3+} ions are hydrated with 7–9 H_2O molecules and the REE chloride complexes are hydrated with 2–7 H_2O molecules, and that the hydration number decreases with an increase in temperature [25–27,30,31,33–35].

Each experimental method used to determine REE speciation has specific challenges. Solubility experiments are an indirect method for determining speciation at hydrothermal conditions [11,12], UV-vis can only be used to determine speciation of colored solutions for REE like Nd, Sm, Eu, and Ho [13–16].Time resolved laser-induced fluorescence spectroscopy (TRLFS) can be used to determine speciation of fluorescent REE, but emission duration and intensity are significantly reduced in aqueous solution at elevated temperatures [17,18,36,37]. Finally, XAFS generally requires access to synchrotron radiation source [25–31].

Raman spectroscopy provides a powerful method for *in situ* characterization of REE speciation in aqueous fluids due to its sensitivity to the intra- and inter- molecular vibrational modes of water and to perturbations in the water structure caused by changes in fluid chemistry and variation of complexing ligands [38–42]. Changes in aqueous REE speciation are derived from the measurement of Raman active bands specific to REE-ligand bonds and water bands related to hydration shells around REE complexes [40,41,43,44]. At low temperature, Raman bands for the REE^{3+} aqua ions are located at 354–406 cm^{-1} [41,45,46] and those for REE chloride species at 221-256 cm^{-1} [19–22,24]. Additionally, *in situ* Raman spectroscopy has been used to derive formation constants for $LuCl^{2+}$ and $YbCl^{2+}$ [22,23] at ambient temperature and for $LaCl^{2+}$ and $LaCl_2^+$ at 5 to 80 °C [24]. Raman spectroscopy may be combined with fused quartz capillary cells [47–49], high pressure-temperature autoclaves with sapphire cells [50–53], or hydrothermal diamond anvil cells [54,55] which allows expanding this method to elevated temperature and pressure relevant for the study of hydrothermal fluids and REE mobilization in ore-forming systems.

In this study, a new capillary Raman heating stage was developed to extend the temperature range of *in situ* Dy speciation experiments in Cl-bearing aqueous solutions from 20 to 300 °C. For identification of the relevant spectral range of the Dy-O and Dy-Cl Raman modes, a series of reference solids including Dy-oxide, -hydroxide, and -chloride were measured. Experiments were performed at ambient temperature and at 50 °C intervals between 100–300 °C for pure water, 1–3 mol/kg NaCl solutions, and experimental solutions with 0.1–1.8 mol/kg dissolved $DyCl_3$. Raman spectra were processed and peak areas for Dy^{3+} aqua ion ($\nu_{1,Dy\text{-}O}$) and Dy chloride complexes ($\nu_{Dy\text{-}Cl}$) were extracted after background solution corrections and compared to predicted Dy speciation using GEM-Selektor [56,57] and current thermodynamic data implemented in the MINES thermodynamic database [58]. This study provides new insights into Dy speciation in acidic fluids at hydrothermal conditions using *in situ* Raman spectroscopy.

Materials and Methods

Materials

The pH stock solutions were prepared using 0.9990 ± 0.0005 mol/L HCl (Inorganic Ventures, NIST traceable certified standard) diluted with ultra pure water (MilliQ, 18.2 MΩ·cm) to make a solution with a pH of 2, 4, and 5. Dysprosium chloride stock solutions were prepared by dissolving solid $DyCl_3 \cdot xH_2O$ (Thermo scientific 99.9% REO basis) in aliquots of the previously prepared pH 2 stock solutions. These Dy stock solutions were subsequently diluted using the pH 2 stock solution to generate a range of Dy concentrations, see Table 1. The NaCl-bearing stock solution was prepared by dissolving high purity sodium chloride (Thermo scientific Puratronic® 99.998% metal basis) in ultra pure water to a concentration of ~3 mol/kg NaCl. This solution

was subsequently diluted using the pH stock solutions and ultra pure water to achieve a range of NaCl concentrations at pH 2, 4, and 5.

Commercial solids analyzed in this study are anhydrous $DyCl_3$ (Strem Chemicals, 99.9% REO), $DyCl_3 \cdot xH_2O$ (Thermo scientific, 99.9% REO basis), and Dy_2O_3 (Alfa Aesar, REacton™ grade, 99.99% REO). The $Dy(OH)_3$ powder used for Raman analysis was synthesized according the method of Diakonov et al. [59]. Pure Dy_2O_3 powder (Alfa Aesar, REacton™ grade, 99.99% REO) was mixed with ultra pure water in a Teflon-lined steel acid digestion vessel (Parr 4744) that was sealed and placed in a muffle furnace (Cole-Palmer Stable Temp muffle furnace, EW-33858-80) where it was allowed to react for up to 21 days at 250 °C.

Analytical Methods

The pH of the dilute stock solutions was measured using a 913 Metrohm pH meter (accuracy of ± 0.003) equipped with a pH electrode (Metrohm 6.0260.010 unitrode with Pt1000 temperature sensor) calibrated using 1.68, 4.01, and 7.00 Fisher buffer solutions (accuracy of ±0.01). The pH of the high ionic strength solutions was measured before the salts were added and calculated using the GEMS code package [56,57,60,61] based on the measured Dy and Na concentrations and amounts of salts added (Table 1).

Dissolved Dy and Na concentrations in the experimental solutions were measured using an Agilent 5900 inductively coupled plasma optical emission spectroscope (ICP-OES) equipped with an advanced valve system (AVS) for sample introduction at the Analytical Chemistry Laboratory in the New Mexico Bureau of Geology and Mineral Resources. An internal standard containing 10 ppm In (SCP Science, NIST traceable) was used for drift corrections. The experimental solutions were acidified to a 2 wt% HNO_3 matrix (trace metal grade, Fisher

Chemical) and diluted to concentrations ranging between 2–5 ppm Na and of 200–400 ppb Dy. Matrix-matched external calibration standards were prepared by dilution of a 10.01 ± 0.04 ppm Dy stock solution (CMS-1, Inorganic Ventures) and a 1002 ± 4 ppm Na stock solution (CGNA1 Inorganic Ventures). The analytical precision (95% confidence level) based on repeated standard analysis was better than 1% for Dy measured using the 353.2 nm wavelength at concentrations between 6×10^{-7} and 5×10^{-6} mol/kg Dy (100–500 ppb) and better than 3% for Na measured using the 589.0 nm wavelength at concentrations between 5×10^{-5} and 2×10^{-4} mol/kg Na (1.3–5.1 ppm). The instrument limits of detection (LOD) were determined as the 5σ (standard deviation) from repeat analysis of the 2 wt% HNO_3 blank, yielding 1 ppb Dy and 0.01 ppm Na. The ICP Expert software was used for data reduction and analysis.

Characterization of the synthetic $Dy(OH)_3$ powder was carried using powder X-ray diffraction (XRD) performed on a Panalytical X-Pert Pro diffractometer at the New Mexico Bureau of Geology and Mineral Resources. A Cu-Kα radiation was used to scan powders from 5 to 70° 2θ angles with a step size of 0.01° 2θ and a step time of 0.3s. The XRD pattern was analyzed using Panalytical HighScore Plus software. Lattice parameters for the synthetic $Dy(OH)_3$ powder derived from Rietveld refinement of the XRD pattern and reported in Smith-Schmitz and Gysi [62] are consistent with those published in Beall et al. [63] (ESI Table S1) and indicate the formation of pure crystalline Dy hydroxide with a hexagonal crystal structure in the $P6_3/m$ space group.

All solids were analyzed using Raman spectroscopy and the main peaks are summarized in Table 2 and reference spectra are summarized in the Electronic Supplementary Information (ESI Table S2). Raman spectroscopy was carried out at the Raman Spectroscopy Laboratory at the New Mexico Bureau of Geology and Mineral Resources using a Horiba LabRAM HR

Evolution confocal microscope. The Raman systems is equipped with a 532 nm excitation Nd:YAG laser and an air cooled diode-pumped solid state 266 nm (UV) excitation laser. Analysis of the solid Dy reference materials was performed using the 266 nm laser and an Olympus 10x LUVB objective (NA = 0.24; WD = 15 mm) and 2400 grooves/mm grating with a spectral resolution of 2 cm^{-1}. Analysis using the 532 nm excitation laser was performed using a 1800 grooves/mm grating with a spectral resolution of 0.2 cm^{-1} and an Olympus 50x LWD objective (NA = 0.5; WD = 10.6 mm) for the solids and an Olympus 20x SLMPLN objective (NA = 0.25; WD = 25 mm) for capillary cell experiments. The Raman spectrometer was calibrated using a first-order C line in diamond at 1332 cm^{-1} for the 266 nm excitation line and an in-line standard reference objective (SP-RCO, Horiba, polystyrene) at 1000.0 cm^{-1} and a first-order Si line at 520.7 cm^{-1} (silicon wafer) for the 532 nm laser. The instrument was calibrated before and after analyses to check for instrument drift and both analyses consistently fell within $\pm$ 0.8 cm^{-1}

Experimental Method for Solutions

The capillary Raman heating stage (Fig. 1) presented in this study was specifically developed to conduct experiments at elevated temperatures and make *in situ* measurements of the Raman modes of Dy species in aqueous solutions. Capillary cells were made using fused quartz capillary tubing (Technical Glass Products, Inc.) with a 2 mm outer diameter and 1 mm inner diameter. The tubes were cut to 11 cm lengths then cleaned in a 5 wt% nitric acid solution and rinsed with pure water. One end of each tube was welded using an acetylene torch, then the tubes were loaded with sample solution to less than 70% of the total volume. Loaded tubes were centrifuged to ensure that the sample solution was collected at the sealed end of the tubes and position of the

meniscus was marked on each tube. The tubes are placed into a liquid nitrogen bath to freeze the liquid before they were sealed. The capillary cells were centrifuged after sealing to ensure that the solution volume was unchanged and no leakage occurred. The capillary cells were then heated to 300 °C in a muffle furnace to ensure that they would not break during the Raman experiments, which were subsequently performed. A small vapor bubble is observed to remain in the capillaries at 300 °C, indicating that the solutions are at saturated water vapor pressure during the experiments. Examination of the capillaries under an optical microscope showed that they were free of solids and clouding both before and after heating experiments.

The capillary Raman heating stage was machined from a block of aluminum alloy (6061-T6511-Extruded, Online Metals) as illustrated in Figure 1. The capillary cells are placed in a 4.5 mm diameter channel with open ends drilled through the block. Two stainless steel 150 W cartridge heaters (Omega, 6.35 mm OD and 10.16 cm length) are inserted into the channels drilled parallel to the capillary cell placed optimally for the best heat distribution. A 2 mm diameter window was drilled orthogonally to the capillary channel to allow Raman analysis. The temperature during experiments was monitored using a high temperature K-type thermocouple (Super OMEGACLAD^{TM}XL, 1.57mm OD, 7.62 cm length) inserted into an oblique channel that reaches the capillary cell close to the Raman window allowing for accurate temperature measurements. The heating cartridges and thermocouple are attached to a 1/16 DIN Omega High Performance Temperature Controller (part# CN16DPT-220) used to regulate and record the temperature during the experiments. The capillary Raman heating stage was wrapped in multiple layers of ceramic pads (Fisher Scientific, GSC Go Science Crazy CP510) for insulation. Temperature testing using multiple thermocouples above and below the capillary at the Raman window indicate that the temperature measured using the K-type thermocouples is within 0.2 °C,

and the temperature gradient between the inside and outside of the capillary is negligible. The capillary Raman heating stage is mounted onto the XYZ-stage using a specifically made holder that locks it into place for the duration of the experiments. The Raman window is aligned optically using the transmitted light source and the automated XYZ-stage.

A capillary cell filled with an experimental solution (Table 1) is inserted into the capillary Raman heating stage at ambient temperature. Laser focusing is achieved by performing a vertical Z-scan at 3200-3800 cm^{-1} and the heights (Z) of the XYZ-stage were set to maximize the peak intensity of the water band. The first measurement was collected at ambient temperature. For each isotherm, the capillary Raman heating stage was heated at a rate of less than 10 °C per minute to minimize the risk of decrepitation. At the experimental temperature the capillary cell was equilibrated for 20 min after which the Raman spectra were collected. Replicate analyses at 100 °C indicate that the spectra are reproducible to within ±1 cm^{-1} after ~15 min at constant temperature. Capillaries containing experimental solutions were reanalyzed following multiple heating and cooling cycles. The final peak positions and normalized intensities were consistent and within analytical uncertainty of those collected initially.

Data Analysis

Raw Raman spectra are exported as text files and background correction, area normalization, and de-convolution are carried out using the Fityk 1.3.1 open-source software [64]. Prior to processing in Fityk the raw aqueous spectra are smoothed using a 14-point Savitzky-Golay algorithm to improve background subtraction for low intensity peaks. The raw spectra ($I(\nu)$) are corrected to remove the influence of temperature and excitation wavelength on the spectral band shape and intensity [41,65–67] producing the reduced spectra ($R(\nu)$) according to,

$$R(\nu) = I(\nu) \cdot B \cdot F_{\nu} / \rho \quad (1)$$

where ρ is the density of the fluids at P and T calculated using the IAPS-84 equation-of-state [68]. The term $F_{\nu t}$ represents the combined scattering and frequency factor used to account for the wavenumber dependence of the Raman scattering intensity, which is given by,

$$F_{\nu} = (\nu_0 - \nu_i)^{-3} \cdot \nu_i \quad (2)$$

where ν_0 and ν_i are the laser excitation and Raman scattered light in cm^{-1}, respectively [66,67]. The Bose-Einstein thermal population correction factor (B) which adjusts for the temperature dependence of the Stokes-Raman scattering intensity is equal to,

$$B = 1 - \exp(-h \cdot \nu_i \cdot c / k_b \cdot T) \quad (3)$$

where h is Planck's constant in J/Hz; c is the speed of light in cm/s; k_b is Boltzmann's constant in J/K; and T is temperature in Kelvin.

All spectra are background subtracted and spectra of aqueous solutions were normalized using the total spectral area to adjust for variation in intensity arising from differences in laser focus depth within the capillaries in Fytik. Normalization using the total spectral area dominated by the area of the water stretching band was previously described in Schmidt and Seward [42] for S species. Aqueous experimental solutions were reduced to two regions of interest at 75–475 cm^{-1} for REE speciation and 2600–4000 cm^{-1} for the main water band. The peaks were de-convoluted using Gaussian functions for aqueous solutions and using a combination of Lorentzian and Gaussian functions for solids based on the best fit for the peaks. The water stretching band was fitted using three peaks (S-1 to S-3, ESI Fig. S1A, B), the librational region was fitted with one peak near 370 cm^{-1} (L-1). The fitted peak centers, peak areas, and full width half maxima (FWHM) are listed in ESI Tables S3-5.

Results and Discussion

Raman Spectra of reference Dy solids

Raman spectra of the Dy-bearing solids including Dy_2O_3(s), $Dy(OH)_3$(s) and anhydrous and hydrous $DyCl_3$, were measured at ambient temperature using two laser excitation wavelengths (532 nm and 266 nm). The reference spectra of different solids were used to establish the main vibrational modes for Dy-O and Dy-Cl bonds, which is needed for interpretation of aqueous solutions. The Raman analyses of Dy-bearing solids measured in this study are summarized in Table 2 and representative Raman spectra for each solid are shown in Figure 2.

Dysprosium sesquioxide occurs in the C-type bixbyite crystal structure and belongs to the Ia-3 space group, where Dy is coordinated with six oxygen [69,70]. Using theoretical calculations, 22 Raman active modes; $4A_g + 4E_g + 14F_g$ were predicted in previous studies [69,71–75], of which 1–17 Raman modes were previously measured [69,71,73,74,76–80]. The spectra is dominated by one Raman mode at 372 ± 1.2 cm^{-1} with a number of minor peaks between ~90 and 600 cm^{-1} (See Hurtig et al. [80] for more details), which is consistent with measurements in this study. The Raman mode at 372 ± 1.2 cm^{-1} corresponds to the symmetric stretching vibration (ν_s) of Dy-O bond and is generally assigned to F_g [75] or F_g+A_g [81].

Dysprosium hydroxide, $Dy(OH)_3$(s), has a hexagonal crystal structure and belongs to the $P6_3/m$ space group with Dy showing a 9-fold coordination with oxygen [63]. Factor group analysis predicts 11 Raman active modes: $4A_g+2E_{1g}+5E_{2g}$ [82]. Previous studies measured between three and 21 bands for Dy hydroxide, comprising of a group of three main peaks between 302 – 488 cm^{-1}, a double peak at 696 and 737 cm^{-1}, peaks at 262 and 133 cm^{-1} and 13 small peaks below 130 cm^{-1} [80,83]. Additionally, $Dy(OH)_3$ has a prominent Raman band at 3598 cm^{-1} with a shoulder at 3612 cm^{-1} that arises from the vibrational modes of the O-H bond [80]. The three most prominent

Raman bands are related to A_g at 312 cm^{-1}, A_g or E_{2g} at 394 cm^{-1} with a shoulder at 406 cm^{-1} and E_{1g} at 501 cm^{-1} of the Dy-OH bond [80,82–85], which are consistent with measurements made in this study.

The anhydrous Dy trichloride $DyCl_3$(s) occurs in the monoclinic crystal structure belonging to the C2/m space group [86]. The Dy ion is 6-fold coordinated with chloride ions showing three pairs of Dy-Cl bonds with unique bond distances [86]. Factor group analysis predicts 12 Raman active modes: $6A_g+6B_g$ [87]. In this study $DyCl_3$(s) was analyzed using the 266 nm excitation laser, due to photoluminescence using the 532 nm excitation laser (Fig. 2C). The strongest peak for $DyCl_3$(s) occurs at 242 cm^{-1} with a shoulder at 255 cm^{-1} and a smaller shoulder at 272 cm^{-1} and can be attributed to the vibrational modes of the Dy-Cl bond consistent with previous studies [87–89]. Dysprosium trichloride is hygroscopic and shows minor peaks at 3200–3600 cm^{-1} corresponding to the Raman mode of water. As a result of hydration minor Dy-H_2O stretching modes (~300–400 cm^{-1}) may also occur [90].

Hydrated Dy chlorides ($DyCl_3 \cdot xH_2O$) can incorporate x = 6–15 water molecules [10,90], of which $DyCl_3 \cdot 6H_2O$ is stable at ambient temperature. The crystal structure of $DyCl_3 \cdot 6H_2O$ is monoclinic belonging to the P2/n space group [89–91]. Dysprosium is 8-fold coordinated with two Cl and six water in a $[DyCl_2(H_2O)_6]^+$ polyhedron with the remaining Cl^- ion acting as a counter anion connecting the cation polyhedra through six hydrogen bonds. Factor group analysis predicts 66 Raman active modes ($32A_g+34B_g$) with 20–28 Raman bands measured in previous studies [89–91]. The bands for vibrational modes involving Dy-Cl and Dy-O bonds are located in the low frequency region at 314–360 cm^{-1} for Dy-H_2O stretching modes and at 159 and 240 cm^{-1} for the symmetric and asymmetric Dy-Cl stretching modes, respectively. Minor modes at ~210 cm^{-1}

and ~94–140 cm^{-1} can be associated to O-Dy-O bending modes and O-Dy-Cl and Cl-O-Cl bending modes [90].

In summary, Raman spectroscopy of reference Dy solids indicate that Raman bands for Dy-O stretching modes occur at 311–502 cm^{-1} and for Dy-Cl stretching modes at 153–272 cm^{-1} (Table 2; Fig. 2). The bands for Dy-O and Dy-Cl are therefore distinct and easily identifiable in their respective positions.

Raman spectra of water at 20–300 °C

Raman spectra of pure water (MilliQ) and H_2O-NaCl-HCl background solutions were collected to distinguish them from the effect of Dy speciation on the Raman spectra for experimental solutions spectra collected at 20–300 °C. The most prominent Raman bands (Fig. 3) correspond to vibrational modes of H_2O, identified as the water translational region at 50–300 cm^{-1}, water librational modes (L) at ~300–1000 cm^{-1}, the water bending mode at 1600–1650 cm^{-1} and the water stretching mode (S) at 3000–3800 cm^{-1} [41,92–95]. The addition of $DyCl_3$ in solution shows a similar shape of the water bands compared to NaCl-bearing solutions with a distinct peak at ~370 cm^{-1} in the region of Dy-O bonds (Figs. 3, 4).

The translational region of water at 50–300 cm^{-1} overlaps significantly with the region of interest for the Raman modes of Dy-Cl bonds at ambient temperature (Fig. 4). The translational region of water comprises information on the structures of networked water as a whole, which can be separated into the lower frequency bending (61 cm^{-1}) and torsion (83 cm^{-1}) restricted translational modes, and higher frequency asymmetric (111 cm^{-1}) and symmetric (157 cm^{-1}) stretching restricted translational modes combined with a coupled translation/rotation mode at 221 cm^{-1} [39,94]. With increasing temperature, the bending and torsion translational modes remain

307 relatively constant, whereas the stretching restricted translation and coupled translation/rotation
308 modes (111–221 cm^{-1}) shift to lower frequency and decrease in intensity [39,92,96,97]. The high
309 frequency edge of the translational region shifts from ~300 cm^{-1} at 25 °C to ~190 cm^{-1} at 300 °C
310 (Fig. 4A, C, E), which decreases the overlap with the region for Dy-Cl vibrational modes at high
311 temperature (Fig. 4E).

312 Librational modes of water centered at 430–480, 550–650, and 720–790 cm^{-1} at 25 °C are
313 weak broad bands arising from limited rotational movement of water molecules within the water
314 network [41,92,97]. The intensities of the librational modes of liquid water decrease with temperature
315 up to 100 °C after which the intensities remain relatively constant [92,97]. In this study, two broad
316 low-intensity peaks appear at ~370 cm^{-1} (L-1) at 100 °C and at ~300 cm^{-1} (L-2) at 250 °C (Fig.
317 4A), which may represent the lower frequency librational modes of water [97]. The L-1 peak can
318 overlap with the region for Dy-O bonds ($\nu_{1,Dy\text{-}O}$) and a correction needs to be applied to Dy-O
319 vibrational modes based on measurements of the background electrolyte solutions. The minor
320 librational mode at 370 cm^{-1} (L-1) was therefore determined in the pure water and background
321 solutions for each temperature and is applied to subsequent solutions as an area normalized
322 contribution, which is described in ESI Tables S3 and S5.

323 The water stretching band at 3000–3800 cm^{-1} is a broad band that represents
324 intramolecular stretching vibrations of the O-H bond [41,93,98–100]. Here, the stretching band is de-
325 convoluted using three sub-peaks i.e., sub-peak S-1 at 3271 cm^{-1}, sub-peak S-2 at 3446 cm^{-1} and
326 sub-peak S-3 at 3588 cm^{-1} at 25 °C (ESI Fig. S1A, B; Table S4). The stretching vibrational band
327 of water is strongly influenced by hydrogen bonding and the structure of water clusters, which
328 indicates that sub-peak S-1 at lower wavenumbers represents fully networked bulk water, sub-
329 peak S-2 is intermediate with smaller hydration clusters and sub-peak S-3 at the highest

wavenumbers represents the weakest hydrogen bonding and smallest monomer and dimer clusters [41,99,100]. With increasing temperature, the water band decreases in intensity and is shifted to higher wavenumbers (Fig. 4B), which indicates decreasing hydrogen bond networks [99,101]. The relative area of sub-peak S-1 decreased from 59% to 6%, sub-peak S-2 increases from 26% to 73% and sub-peak S-3 increases from 15% to 21% from 20 to 300 °C. Sub-peak 2 also shifts to higher wavenumbers which indicates a greater overlap with sub-peak S-3 at high temperatures and the dominance of smaller hydrogen clusters.

The effect of chlorinity on the water on Raman spectra at 20–300 °C

In the translational region, the addition of NaCl shifts the high frequency edge by ~10 cm^{-1} to lower wavenumbers at ambient temperature (Fig 4A, C). The high frequency edge of the translational region shifts to lower wavenumbers and decreases in intensity with increasing temperature in NaCl-bearing and pure water. The librational modes at ~300, 370 and 450 cm^{-1} occur in NaCl-bearing solutions and pure water above 100 °C as low intensity broad peaks.

The addition of NaCl affects the water stretching band by decreasing the intensity of sub-peak S-1 at 3271 cm^{-1} and increasing sub-peak S-2 at 3446 cm^{-1} accompanied by a very slight decrease in sub-peak S-3 at 3584 cm^{-1} [41,102–106]. The sub-peaks changes are proportional to the concentration of NaCl in solution (Fig. 5B, D; ESI Table S4), indicating that the addition of NaCl breaks up hydrogen bond networks in water [40,41,105]. At ambient temperature, the relative sub-peak contributions to the water band systematically shift as a function of NaCl (Fig. 5A). Sub-peak 1 is the largest peak in pure water and gradually decreases with increasing NaCl content, whereas sub-peak 2 increases until they are of similar peak areas at ~3 mol/kg NaCl. Sub-peak 3 is the smallest peak and remains constant in peak area contribution as a function of

353 NaCl concentration. The water stretching bands show a decrease in relative peak areas of sub-
354 peak S-1 from 41-51% to 7-8% and a corresponding increase in relative areas of sub-peak S-2
355 from 34-45% to 78-82% with increasing temperature from 20–300 °C (Fig. 5; ESI Table S4). At
356 300 °C, sub-peak 2 is the largest peak and contributes an increasing percentage to the water band
357 with increasing NaCl content (Fig. 5B), whereas the second largest peak is S-3, which decreases
358 in peak area contribution with increasing NaCl content. Sub-peak 1 is the smallest peak at high
359 temperature and increases with increasing NaCl content. The effect of salinity on the relative
360 contributions of sub-peaks S-1 and S-2 decrease significantly at elevated temperatures and the
361 total peak shape of NaCl-bearing solutions starts to resemble that of pure water. This observation
362 is consistent with increased species association and the formation of aqueous $NaCl^0$ at high
363 temperature resulting in less perturbation to the local water structure [107]. Prediction of Na
364 speciation using the $NaCl^0$ association constant from Miron et al. [108] indicates that the proportion
365 of $NaCl^0$ increases significantly between 25 and 300 °C, from 6.9% to 37% of total dissolved Na
366 in a 1 mol/kg NaCl solution and from 19% to 47% in a 2.9 mol/kg NaCl solution (ESI Fig. S2),

367 Chloride in $DyCl_3$-bearing solutions causes systematic perturbations to the water
368 stretching band similar to those observed for NaCl-bearing solutions (Figs. 4, 5; ESI Table S4),
369 though the effect of added $DyCl_3$ is less pronounced, especially for sub-peaks S-1 and S-2 below
370 200 °C and sub-peaks S-2 and S-3 above 200 °C. The lower correlation between dissolved Cl
371 concentrations and changes to sub-peak contributions in $DyCl_3$-bearing solutions than in the
372 NaCl-bearing solution suggests that Dy chloride species are likely present resulting in less Cl^-
373 available for perturbation of the water structure (Fig. 5). As in the NaCl solutions, with
374 increasing temperature the effect of $DyCl_3$ on the water stretching band becomes less extreme.
375

Raman spectra of $DyCl_3$-bearing solutions as function temperature

In $DyCl_3$-bearing solutions a new peak appears at 378–384 cm^{-1} and increases in intensity with increasing dissolved $DyCl_3$ concentrations at ambient temperature (Figs. 4E, 6A; ESI Fig. S1C, D). The band at 378–384 cm^{-1} is attributed to the Dy-O symmetric stretching mode ($\nu_{1,Dy\text{-}O}$) of the hydrated Dy^{3+} aqua ions in octahedral coordination [19,22,41,46] (Table 4). The Dy-O ($\nu_{1,Dy\text{-}O}$) band systematically shifts to lower wavenumbers from 384 cm^{-1} in the 0.14 mol/kg $DyCl_3$ solution to 378 cm^{-1} in the 1.8 mol/kg $DyCl_3$ solution, indicating a change in coordination chemistry of the hydration shell (Fig. 6A, Table 4). The shift of REE-O bands to lower wavenumbers with increasing $REECl_3$ concentrations has been attributed to Cl^- ions changing the hydration shells of the REE^{3+} aqua ions at ambient temperature [19–23]. At ambient temperature, the area of the Dy-O ($\nu_{1,Dy\text{-}O}$) band increases near linearly with increasing $DyCl_3$ concentration (Fig 7A, Table 4). The band at 240 cm^{-1} corresponding to the Dy-Cl bond [19,22], is overprinted by the translational mode of water at room temperature and appears as a shoulder of increasing intensity on the translational water band with increasing dissolved $DyCl_3$ concentrations (Fig. 7A; Table 2).

With increasing temperature, the intensity of the Dy-O band ($\nu_{1,Dy\text{-}O}$) decreases (Figs. 6 and 7B-F). Above 100 °C, the 370 cm^{-1} (L-1) peak occurring in pure water and NaCl-bearing solutions need to be subtracted from the Dy-O band area to distinguish the Dy-O peaks (Table 4; ESI Table S5). The Dy-O band becomes indistinguishable from the librational band of water at 370 cm^{-1} above 150 °C for the 0.14 mol/kg $DyCl_3$ solution, and above 200 °C for the 0.27 mol/kg $DyCl_3$ solution (Fig. 6A, B). The Dy-O band shifts systematically from 378 cm^{-1} at ambient temperature to 365 cm^{-1} at 300 °C for the 1.8 mol/kg $DyCl_3$ spectra (Table 4). The Dy-Cl band ($\nu_{Dy\text{-}Cl}$) near 240 cm^{-1} is measurable in the 0.59 to 1.8 mol/kg $DyCl_3$ solutions at 100 °C,

399 however, the Dy-Cl band in the 0.14 and 0.27 mol/kg $DyCl_3$ solutions is indistinguishable from
400 noise observed in the background spectra at 100 °C. The Dy-Cl band becomes measurable in all
401 $DyCl_3$ solutions above 150 °C and its intensity increases systematically with increasing
402 temperature (Fig. 6B-F).

403 The Dy-Cl band position measured in this study is consistent with Rudolph and Irmer [19–
404 23] who report a chloride band at 228 cm^{-1} for $[La(H_2O)_{9-n}Cl_n]^{3-n}$, 245 cm^{-1} for $[Ce(H_2O)_{9-n}Cl_n]^{3-n}$,
405 248 cm^{-1} for $[Y(H_2O)_{8-n}Cl_n]^{3-n}$, 254 cm^{-1} for $[Lu(H_2O)_{8-n}Cl_n]^{3-n}$, and 256 for $[Yb(H_2O)_{8-n}Cl_n]^{3-n}$,
406 with n = 1 or 2. Conversely, Ghosh et al. [41] attributes the band measured at 239 cm^{-1} in a 0.17 M
407 $DyCl_3$ solution to intermolecular H-bond stretching band, which is shifted to lower wavelengths
408 due to the presence of a Dy^{3+} ion at ambient temperature. However, based on the reference Dy
409 solids measured in this study (Fig. 2) we interpret the peak measured at 240 cm^{-1} (Fig. 5) to
410 represent the Dy-Cl stretching mode and attribute the bands at 363–384 cm^{-1} to represent the
411 hydrated Dy^{3+} aqua ion in accordance with Rudolph and Irmer [19–23]. Persaud et al. [24], used two
412 Gaussian sub-peaks to fit the broad band at ~230 cm^{-1} in their La chloride solutions to estimate
413 two La chloride species. In this study one Gaussian peak was used to fit the Dy-Cl band (ESI
414 Fig. S1C, D) because a single peak provides a better overall fit to the Dy-Cl peak shape;
415 therefore we do not distinguish two chloride species.

416 Examination of the Dy-O ($A_{Dy\text{-}O,corr}$; corrected for the area contribution of L-1) and Dy-Cl
417 ($A_{Dy\text{-}Cl}$) peak areas (Table 4, ESI Table S5) show that peak intensity appears to increase near
418 linearly with increasing dissolved $DyCl_3$ concentrations at all temperatures (Fig. 7A, C).
419 However, closer examination shows that the slope of $A_{Dy\text{-}O,corr}$ decreases and the slope of $A_{Dy\text{-}Cl}$
420 increases with increasing $DyCl_3$ concentration and temperature, indicating a higher affinity to
421 form Dy chloride complexes in the more concentrated solutions [19–23]. The Dy-O band becomes

indistinguishable from background at concentrations below 0.59 mol/kg $DyCl_3$ at a temperature of 250 °C and above (Fig. 7A). Conversely, the Dy-Cl band only becomes quantifiable at a temperature above 100 °C (Fig. 7B). This behavior is interpreted to indicate increased formation of Dy chloride complexes. With increasing temperature, the Dy-O peaks decrease with near linear slopes, whereas the Dy-Cl peaks increase exponentially (Fig. 7B,D).

Dy speciation as a function of temperature and chlorinity

Speciation of Dy in the experimental fluids was simulated using the GEM-Selektor code package [56,57,60,61] and the MINES thermodynamic database [58]. The thermodynamic data for the aqueous species in the Dy-Cl-O-H system is summarized in ESI Table S6. The TSolMod library [109] was used for all activity and equation of state calculations and the revised HKF equation-of-state [110–113] was used to calculate the thermodynamic properties of aqueous species at elevated temperature (for more details see ESI).

Four experimental solutions with $DyCl_3$ concentrations of 0.14, 0.27, 0.59, and 1.8 mol/kg and an acidic starting pH of 2 were simulated at temperatures between 25 and 300 °C (Fig. 8). At the lowest $DyCl_3$ concentration, Dy speciation is dominated by the Dy^{3+} ion at low temperature and Dy chloride species at temperatures above 200 °C (Fig 8A). The Dy chloride species become more stable with increasing dissolved $DyCl_3$ concentrations and dominate Dy speciation above 195 °C in 0.27 mol/kg $DyCl_3$, 175 °C in 0.59 mol/kg $DyCl_3$, and 25 °C in 1.8 mol/kg $DyCl_3$ solutions (Fig. 8B, C, D).

At ambient temperature, Dy chloride species could not be identified using *in situ* Raman spectroscopy due to the overlap of the translational water region with the Dy-Cl peak. The Dy^{3+} aqua ion is identified in all experimental solutions at ambient temperature (Fig. 6A), which is

consistent with thermodynamic simulations indicating that Dy^{3+} contributes nearly 50 mol% to the total dissolved Dy concentration in the 1.8 mol/kg $DyCl_3$ solution and more than 75 mol% in the less concentrated $DyCl_3$ solutions (Fig. 8). The peak center position of the Dy-O band shifts to lower wavenumbers with increasing dissolved $REECl_3$ concentrations at ambient temperature (Fig. 9). This shift indicates that Cl^- affects the Dy^{3+} hydration shells [19,22] (Fig. 9). The effect of Cl on inner and outer hydration shells cannot be simulated using the thermodynamic equilibrium approach presented in Figure 8, which is limited to Dy chloride species based on thermodynamic data available in the literature; the chloride species are generally modeled as stable inner sphere chloride complexes in macroscopic thermodynamics vs. molecular models.

Comparison of molar ratios ($M_{DyCl,total}/M_{Dy3+}$) from thermodynamic calculations to measured peak area ratios ($A_{Dy\text{-}Cl}/A_{Dy\text{-}O}$) from *in situ* Raman spectroscopy (Fig. 10) provides a qualitative measure of the accuracy of thermodynamic predictions. Importantly, the scattering coefficients for Dy chloride and Dy^{3+} species are unknown as is their behavior with increasing temperature. If they are assumed to be similar, then area ratios can be directly compared to molar ratios from simulations. However, the peak areas of Dy-Cl increase exponentially and Dy-O decrease linearly with increasing temperature, indicating that the scattering coefficients are likely temperature-dependent and different for Dy^{3+} and Dy chloride species. Determination of scattering coefficients from Raman spectra requires internal calibration using solutions having only one REE complex present as shown in previous studies [22,24].

In situ Raman spectroscopy indicates that the Dy chloride species become dominant above 200 °C in all experimental solutions, which is in agreement with thermodynamic predictions for the $DyCl_3$-bearing solutions with lowest $DyCl_3$ concentration (0.14 mol/kg $DyCl_3$), whereas the model starts to deviate in more concentrated solutions (Fig. 10). The

468 increased $DyCl_3$ content of the solutions shifts the Dy chloride predominance field to lower
469 temperature. However, the Dy^{3+} aqua ion is more stable than the Dy chloride species below 200
470 °C. The greater stability of REE^{3+}relative to REE chloride species at low temperature is
471 consistent with other *in situ* Raman spectroscopy studies [22,24].
472
473 **Conclusions**
474 The speciation of Dy^{3+} aqua ion and Dy chloride complexes were measured *in situ* at elevated
475 temperature 20–300 °C and a range of dissolved $DyCl_3$ concentrations providing new insights
476 into the speciation dominance fields at hydrothermal conditions. Peak center positions for Dy-O
477 ($\nu_{1,Dy\text{-}O}$) Raman modes were identified at 365–384 cm^{-1} and for Dy-Cl ($\nu_{Dy\text{-}Cl}$) near 240 cm^{-1} in
478 aqueous solutions corresponding to the hydrated Dy^{3+} aqua ion, i.e., $[Dy(H_2O)_8]^{3+}{}_{(aq)}$ and the Dy
479 chloride complexes, respectively. A systematic decrease in wavenumber of the Dy-O peak with
480 increasing $DyCl_3$ concentrations at ambient temperature indicates the replacement of water with
481 Cl^- ions in the hydration shells of the Dy^{3+} aqua ion. A separate peak for the Dy-Cl bond appears
482 as a shoulder on the translational mode of water at ambient temperatures, as a discrete peak at
483 100 °C that becomes the major peak above 200 °C, indicating the presence and subsequent
484 dominance of inner sphere Dy chloride complexes in aqueous solutions with increasing
485 temperature.
486 Comparison of the relative abundance of *in situ* measured Dy^{3+} aqua ion and Dy chloride
487 species using the ratio of $A_{Dy\text{-}O}/A_{Dy\text{-}Cl}$ to predicted ratios of molar concentrations
488 ($M_{Dy3+}/M_{DyCl,tot}$) indicate that the available thermodynamic models overestimate the stability of
489 Dy chloride complexes at low temperature and high salinities (Fig. 10). Above 200 °C,

thermodynamic predictions are in accordance with the Raman experiments and indicate that Dy chloride complexes are the primary Dy species in acidic chloride bearing aqueous fluids.

These findings indicate the need for further research to improve the thermodynamic properties of Dy chloride species and the Dy^{3+} aqua ion in acidic Cl-bearing hydrothermal fluids. This study provides a benchmark for expanding the use of *in situ* Raman spectroscopy applied to REE speciation in aqueous solutions to hydrothermal conditions. Importantly, the change in species dominance between the Dy^{3+} aqua ion and Dy chloride species could be quantified experimentally in acidic solutions as a function of temperature, providing new insights that were not possible to obtain using other experimental techniques.

Acknowledgments

The experimental research was supported by the U.S. Department of Energy, Office of Science, Office of Basic Energy Sciences, Geosciences program under Award DE-SC0022269 to AG and NH. The Raman Spectrometer was purchased with NSF grant EAR-MRI-2117061 to NH and AG. The authors would like to thank New Mexico Tech colleagues Bonnie Frey and Hannah Han for their assistance with ICP-OES analyses and Bryan Maciag for interesting discussions about method development. We are grateful to two anonymous reviewers for their constructive reviews. We also thank Dr. Vadapalli Chandrasekhar for the editorial handling.

Author Contributions

SS – Writing, Original draft, Methodology, Formal analysis, Validation, Investigation, Conceptualization, Data curation. AG and NH – Conceptualization, Funding acquisition,

Supervision, Resources, Writing, Review and Editing, Validation, Investigation, Data Curation, Methodology.

Conflicts of interest

There are no conflicts to declare.

References

1 N. G. Connelly, Royal Society of Chemistry (Great Britain), and International Union of Pure and Applied Chemistry, Eds., *Nomenclature of inorganic chemistry. IUPAC recommendations 2005*, Royal Society of Chemistry Publishing/IUPAC, Cambridge, UK, 2005.

2 B. Zhou, Z. Li and C. Chen, *Minerals*, 2017, **7**, 203.

3 B. J. Smith and R. G. Eggert, *Environ. Sci. Technol.*, 2018, **52**, 3803–3811.

4 B. Smith, M. Riddle, M. Earlam, C. Iloeje and D. Diamond, *Rare Earth Permanent Magnets: Supply Chain Deep Dive Assessment*, 2022.

5 Y. Liang, R. Kleijn, A. Tukker and E. Van Der Voet, *Renew. Sustain. Energy Rev.*, 2022, **161**, 112334.

6 U.S. Department of Energy, Notice of Final Determination on 2023 DOE Critical Materials List, (accessed July 1, 2024).

7 A. Migdisov, A. E. Williams-Jones, J. Brugger and F. A. Caporuscio, *Chem. Geol.*, 2016, **439**, 13–42.

8 A. P. Gysi, A. E. Williams-Jones and P. Collins, *Econ. Geol.*, 2016, **111**, 1241–1276.

9 A. K. Patel, D. Upadhyay, B. Mishra and K. L. Pruseth, *Lithos*, 2023, **444–445**, 107097.

10 G. Das, M. M. Lencka, A. Eslamimanesh, A. Anderko and R. E. Riman, *Fluid Phase Equilibria*, 2017, **452**, 16–57.

11 Art. A. Migdisov, A. E. Williams-Jones and T. Wagner, *Geochim. Cosmochim. Acta*, 2009, **73**, 7087–7109.

12 C. H. Gammons, S. A. Wood and A. E. Williams-Jones, *Geochim. Cosmochim. Acta*, 1996, **60**, 4615–4630.

13 A. A. Migdisov and A. E. Williams-Jones, *Geochim. Cosmochim. Acta*, 2002, **66**, 4311–4323.

14 Art. A. Migdisov and A. E. Williams-Jones, *Chem. Geol.*, 2006, **234**, 17–27.

15 Art. A. Migdisov, A. E. Williams-Jones, C. Normand and S. A. Wood, *Geochim. Cosmochim. Acta*, 2008, **72**, 1611–1625.

16 S. A. Stepanchikova and G. R. Kolonin, *Russ. J. Coord. Chem.*, 2005, **31**, 193–202.
17 T. Kimura and Y. Kato, *J. Alloys Compd.*, 1998, **278**, 92–97.
18 T. Kimura and Y. Kato, *J. Alloys Compd.*, 1998, **271–273**, 867–871.
19 W. W. Rudolph and G. Irmer, *Dalton Trans.*, 2015, **44**, 18492–18505.
20 W. W. Rudolph and G. Irmer, *Dalton Trans.*, 2015, **44**, 295–305.
21 W. W. Rudolph and G. Irmer, *Dalton Trans.*, 2017, **46**, 4235–4244.
22 W. Rudolph and G. Irmer, *Molecules*, 2019, **24**, 1953.
23 W. Rudolph and G. Irmer, *Molecules*, 2018, **23**, 3237.
24 A. A. Persaud, S. Sasidharanpillai, J. S. Cox and P. R. Tremaine, *Can. J. Chem.*, 2024, cjc-2024-0074.
25 R. A. Mayanovic, S. Jayanetti, A. J. Anderson, W. A. Bassett and I.-M. Chou, *J. Phys. Chem. A*, 2002, **106**, 6591–6599.
26 R. A. Mayanovic, A. J. Anderson, W. A. Bassett and I.-M. Chou, *Chem. Geol.*, 2009, **259**, 30–38.
27 M. Louvel, A. Bordage, D. Testemale, L. Zhou and J. Mavrogenes, *Chem. Geol.*, 2015, **417**, 228–237.
28 R. A. Mayanovic, A. J. Anderson, W. A. Bassett and I.-M. Chou, *Chem. Geol.*, 2007, **239**, 266–283.
29 R. A. Mayanovic, A. J. Anderson, W. A. Bassett and I.-M. Chou, *Am. Mineral.*, 2009, **94**, 1487–1490.
30 Q. Guan, Y. Mei, B. Etschmann, M. Louvel, D. Testemale, R. Spezia and J. Brugger, *Geochim. Cosmochim. Acta*, 2022, **330**, 27–46.
31 W. Liu, B. Etschmann, A. Migdisov, H. Boukhalfa, D. Testemale, H. Müller, J.-L. Hazemann and J. Brugger, *Chem. Geol.*, 2017, **459**, 61–74.
32 H. J. Han and A. P. Gysi, *Dalton Trans.*, 2024, **53**, 13129–13141.
33 Q. Guan, Y. Mei, B. Etschmann, D. Testemale, M. Louvel and J. Brugger, *Geochim. Cosmochim. Acta*, 2020, **281**, 168–189.
34 A. J. Anderson, S. Jayanetti, R. A. Mayanovic, W. A. Bassett and I.-M. Chou, *Am. Mineral.*, 2002, **87**, 262–278.
35 R. A. Mayanovic, A. J. Anderson, W. A. Bassett and I.-M. Chou, *Rev. Sci. Instrum.*, 2007, **78**, 053904.
36 P. Lindqvist-Reis, R. Klenze, G. Schubert and T. Fanghänel, *J. Phys. Chem. B*, 2005, **109**, 3077–3083.
37 C. Koke, A. Skerencak-Frech and P. J. Panak, *J. Chem. Thermodyn.*, 2019, **131**, 219–224.
38 G. E. Walrafen, *J. Chem. Phys.*, 1966, **44**, 1546–1558.
39 G. E. Walrafen, Y. C. Chu and G. J. Piermarini, *J. Phys. Chem.*, 1996, **100**, 10363–10372.
40 Y. Marcus, *J. Solut. Chem.*, 2009, **38**, 513–516.
41 N. Ghosh, A. Bandyopadhyay, S. Roy, G. Saha and J. A. Mondal, *J. Mol. Liq.*, 2023, **389**, 122927.

42 C. Schmidt and T. M. Seward, *Chem. Geol.*, 2017, **467**, 64–75.
43 W. W. Rudolph, G. Irmer and E. Königsberger, *Dalton Trans*, 2008, 900–908.
44 Y. Wan, X. Wang, I.-M. Chou and X. Li, *Earth Planet. Sci. Lett.*, 2021, **569**, 117068.
45 H. Kanno, *J. Phys. Chem.*, 1988, **92**, 4232–4236.
46 W. W. Rudolph and G. Irmer, *J. Solut. Chem.*, 2020, **49**, 316–331.
47 L. M. S. G. A. Applegarth, C. Alcorn, K. Bissonette, J. Noël and P. R. Tremaine, *Appl. Spectrosc.*, 2015, **69**, 972–983.
48 I.-M. Chou, R. C. Burruss and W. Lu, in *Advances in High-Pressure Technology for Geophysical Applications*, Elsevier, 2005, pp. 475–485.
49 X. Wang, I.-M. Chou, W. Hu, R. C. Burruss, Q. Sun and Y. Song, *Geochim. Cosmochim. Acta*, 2011, **75**, 4080–4093.
50 M. Louvel, A. Bordage, C. Da Silva-Cadoux, D. Testemale, E. Lahera, W. Del Net, O. Geaymond, J. Dubessy, R. Argoud and J.-L. Hazemann, *J. Mol. Liq.*, 2015, **205**, 54–60.
51 S. Sasidharanpillai, H. Arcis, L. Trevani and P. R. Tremaine, *J. Phys. Chem. B*, 2019, **123**, 5147–5159.
52 J. Conrad and P. R. Tremaine, *Phys. Chem. Chem. Phys.*, 2021, **23**, 10670–10685.
53 S. Sasidharanpillai, J. S. Cox, C. C. Pye and P. R. Tremaine, *Dalton Trans.*, 2023, **52**, 18391–18406.
54 K. Mibe, I. Chou and W. A. Bassett, *J. Geophys. Res. Solid Earth*, 2008, **113**, 2007JB005179.
55 C. Schmidt and A. Watenphul, *Geochim. Cosmochim. Acta*, 2010, **74**, 6852–6866.
56 D. A. Kulik, T. Wagner, S. V. Dmytrieva, G. Kosakowski, F. F. Hingerl, K. V. Chudnenko and U. R. Berner, *Comput. Geosci.*, 2013, **17**, 1–24.
57 G. D. Miron, D. A. Kulik, S. V. Dmytrieva and T. Wagner, *Appl. Geochem.*, 2015, **55**, 28–45.
58 A. P. Gysi, N. C. Hurtig, R. Pan, G. D. Miron and D. A. Kulik, 2023.
59 I. I. Diakonov, B. R. Tagirov and K. V. Ragnarsdottir, *ract*, 1998, **81**, 107–116.
60 I. K. Karpov, K. V. Chudnenko, D. A. Kulik, O. V. Avchenko and V. A. Bychinskii, *Geochem. Int.*, 2001, **39**, 1108–1119.
61 I. K. Karpov, *Am. J. Sci.*, 2002, **302**, 281–311.
62 S. E. Smith-Schmitz and A. P. Gysi, *Chem. Geol.*, 2025, **674**, 122576.
63 G. W. Beall, W. O. Milligan and H. A. Wolcott, *J. Inorg. Nucl. Chem.*, 1977, **39**, 65–70.
64 M. Wojdyr, *J. Appl. Crystallogr.*, 2010, **43**, 1126–1128.
65 M. H. Brooker, O. F. Nielsen and E. Praestgaard, *J. Raman Spectrosc.*, 1988, **19**, 71–78.
66 M. Steele-MacInnis and C. Schmidt, *Geochim. Cosmochim. Acta*, 2014, **136**, 126–141.
67 W. W. Rudolph and G. Irmer, *Appl. Spectrosc.*, 2007, **61**, 1312–1327.
68 J. Kestin, J. V. Sengers, B. Kamgar-Parsi and J. M. H. L. Sengers, *J. Phys. Chem. Ref. Data*, 1984, **13**, 175–183.

69 W. B. White and V. G. Keramidas, *Spectrochim. Acta Part Mol. Spectrosc.*, 1972, **28**, 501–509.
70 S. C. Atkinson, PhD, University of Salford, 2013.
71 J. B. Gruber, R. D. Chirico and E. F. Westrum, *J. Chem. Phys.*, 1982, **76**, 4600–4605.
72 Y. Repelin, C. Proust, E. Husson and J. M. Beny, *J. Solid State Chem.*, 1995, **118**, 163–169.
73 J.-C. Panitz, J.-C. Mayor, B. Grob and W. Durisch, *J. Alloys Compd.*, 2000, **303–304**, 340–344.
74 A. Ubaldini and M. M. Carnasciali, *J. Alloys Compd.*, 2008, **454**, 374–378.
75 M. V. Abrashev, N. D. Todorov and J. Geshev, *J. Appl. Phys.*, 2014, **116**, 103508.
76 L. A. Tucker, F. J. Carney, P. McMillan, S. H. Lin and L. Eyring, *Appl. Spectrosc.*, 1984, **38**, 857–860.
77 N. Dilawar, S. Mehrotra, D. Varandani, B. V. Kumaraswamy, S. K. Haldar and A. K. Bandyopadhyay, *Mater. Charact.*, 2008, **59**, 462–467.
78 X. Fu, Y. Xu and J. Zhou, *J. Mater. Sci.*, 2012, **47**, 1697–1701.
79 J. Yu, L. Cui, H. He, S. Yan, Y. Hu and H. Wu, *J. Rare Earths*, 2014, **32**, 1–4.
80 N. C. Hurtig, A. P. Gysi, S. E. Smith-Schmitz and D. Harlov, *Dalton Trans*, 2024.
81 G. Schaack and J. A. Koningstein, *J. Opt. Soc. Am.*, 1970, **60**, 1110.
82 K. Ahrens, H. Gerlinger, H. Lichtblau, G. Schaack, G. Abstreiter and S. Mroczkowski, *J. Phys. C Solid State Phys.*, 1980, **13**, 4545–4564.
83 S. Liu, Y. Liu, Q. Mu, F. Zhang, H. Li and Y. Wang, *Appl. Phys. A*, 2013, **111**, 1229–1240.
84 Q. G. Zeng, Z. J. Ding, Z. M. Zhang and Y. Q. Sheng, *J. Phys. Chem. C*, 2010, **114**, 4895–4900.
85 S. R. Sanivarapu, J. B. Lawrence and G. Sreedhar, *ACS Omega*, 2018, **3**, 6267–6278.
86 D. H. Templeton and G. F. Carter, *J. Phys. Chem.*, 1954, **58**, 940–944.
87 G. N. Papatheodorou, *J. Chem. Phys.*, 1977, **66**, 2893–2900.
88 A. Chrissanthopoulos and G. N. Papatheodorou, *J. Mol. Struct.*, 2008, **892**, 93–102.
89 I. D. Zakirýanova, V. A. Khokhlov, A. B. Salyulev and I. V. Korzun, *Z. Für Naturforschung A*, 2015, **70**, 153–157.
90 G. Oczko and L. Macalik, *Polyhedron*, 2010, **29**, 1231–1236.
91 G. Oczko, L. Macalik, J. Legendziewicz and J. Hanuza, *J. Alloys Compd.*, 2004, **380**, 327–336.
92 G. E. Walrafen, *J. Chem. Phys.*, 1967, **47**, 114–126.
93 Q. Sun, *Vib. Spectrosc.*, 2009, **51**, 213–217.
94 M. Galvin and D. Zerulla, *ChemPhysChem*, 2011, **12**, 913–914.
95 T. Seki, K.-Y. Chiang, C.-C. Yu, X. Yu, M. Okuno, J. Hunger, Y. Nagata and M. Bonn, *J. Phys. Chem. Lett.*, 2020, **11**, 8459–8469.
96 G. E. Walrafen, M. R. Fisher, M. S. Hokmabadi and W.-H. Yang, *J. Chem. Phys.*, 1986, **85**, 6970–6982.
97 D. M. Carey and G. M. Korenowski, *J. Chem. Phys.*, 1998, **108**, 2669–2675.

98 W. F. Murphy and H. J. Bernstein, *J. Phys. Chem.*, 1972, **76**, 1147–1152.
99 Q. Hu, X. Lü, W. Lu, Y. Chen and H. Liu, *J. Mol. Spectrosc.*, 2013, **292**, 23–27.
100 A. W. Knight, N. G. Kalugin, E. Coker and A. G. Ilgen, *Sci. Rep.*, 2019, **9**, 8246.
101 G. E. Walrafen, W.-H. Yang and Y. C. Chu, *J. Phys. Chem. B*, 1999, **103**, 1332–1338.
102 J. Dubessy, T. Lhomme, M.-C. Boiron and F. Rull, *Appl. Spectrosc.*, 2002, **56**, 99–106.
103 F. Rull, *Pure Appl. Chem.*, 2002, **74**, 1859–1870.
104 Q. Sun, L. Zhao, N. Li and J. Liu, *Chem. Geol.*, 2010, **272**, 55–61.
105 Q. Sun, *Vib. Spectrosc.*, 2012, **62**, 110–114.
106 M. Ahmed, V. Namboodiri, A. K. Singh and J. A. Mondal, *J. Chem. Phys.*, 2014, **141**, 164708.
107 X. Wu, W. Lu, W. Ou, M.-C. Caumon and J. Dubessy, *J. Raman Spectrosc.*, 2017, **48**, 314–322.
108 G. D. Miron, T. Wagner, D. A. Kulik and C. A. Heinrich, *Geochim. Cosmochim. Acta*, 2016, **187**, 41–78.
109 T. Wagner, D. A. Kulik, F. F. Hingerl and S. V. Dmytrieva, *Can. Mineral.*, 2012, **50**, 1173–1195.
110 H. C. Helgeson, D. H. Kirkham and G. C. Flowers, *Am. J. Sci.*, 1981, **281**, 1249–1516.
111 E. L. Shock and H. C. Helgeson, *Geochim. Cosmochim. Acta*, 1988, **52**, 2009–2036.
112 J. C. Tanger and H. C. Helgeson, *Am. J. Sci.*, 1988, **288**, 19–98.
113 E. L. Shock, E. H. Oelkers, J. W. Johnson, D. A. Sverjensky and H. C. Helgeson, *J Chem Soc Faraday Trans*, 1992, **88**, 803–826.
114 E. L. Shock, D. C. Sassani, M. Willis and D. A. Sverjensky, *Geochim. Cosmochim. Acta*, 1997, **61**, 907–950.
115 S. Arunachalam, B. Kirubasankar, V. Murugadoss, D. Vellasamy and S. Angaiah, *New J. Chem.*, 2018, **42**, 2923–2932.

519 **Figures:**

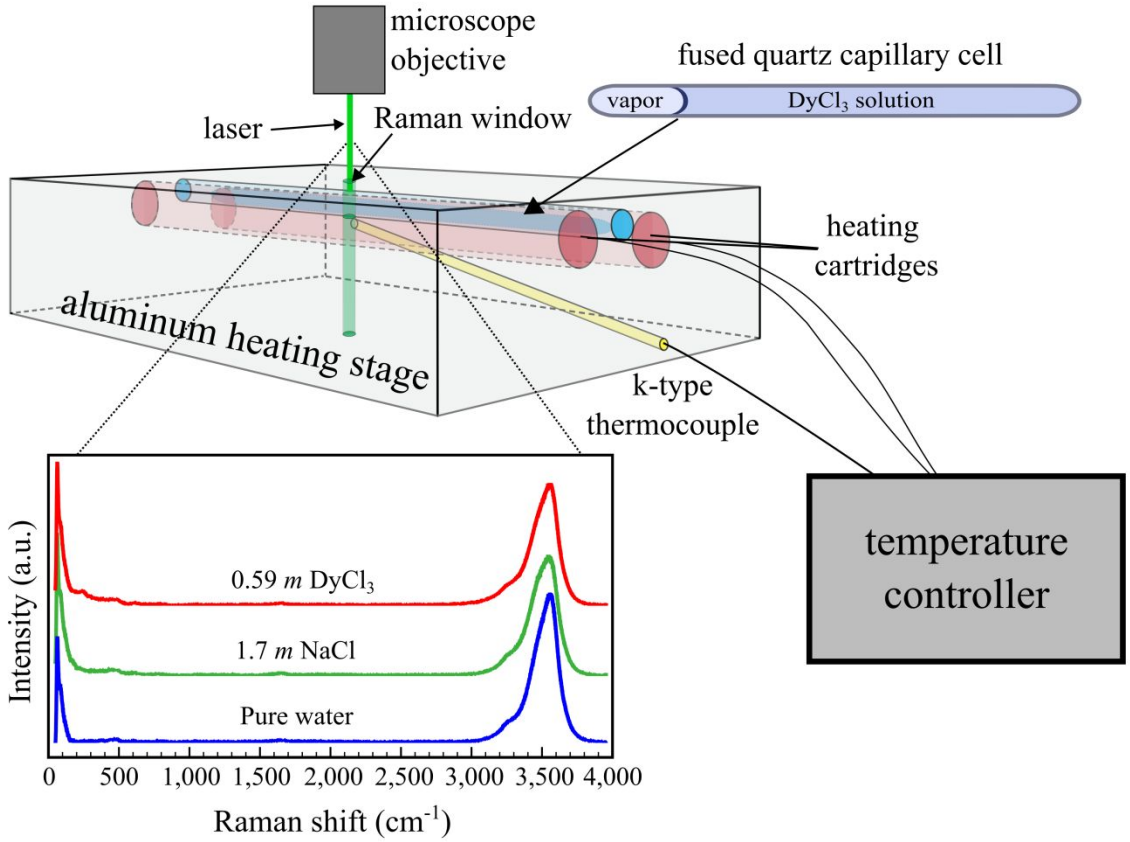

520 **Figure 1:** Schematic diagram of the capillary Raman heating stage used for *in situ* measurement
521 of aqueous Dy speciation at 20–300 °C. The capillary Raman heating stage is made of aluminum
522 and has two 8 mm diameter holes for the heating cartridges, one 4.5 mm hole for the capillary
523 cell and an inclined 2 mm hole for the thermocouple. The capillary cells are made of fused quartz
524 glass and contain an aqueous solution and a vapor bubble. The Raman window crosscuts the cell
525 in the center to allow for Raman analysis of experimental solutions.

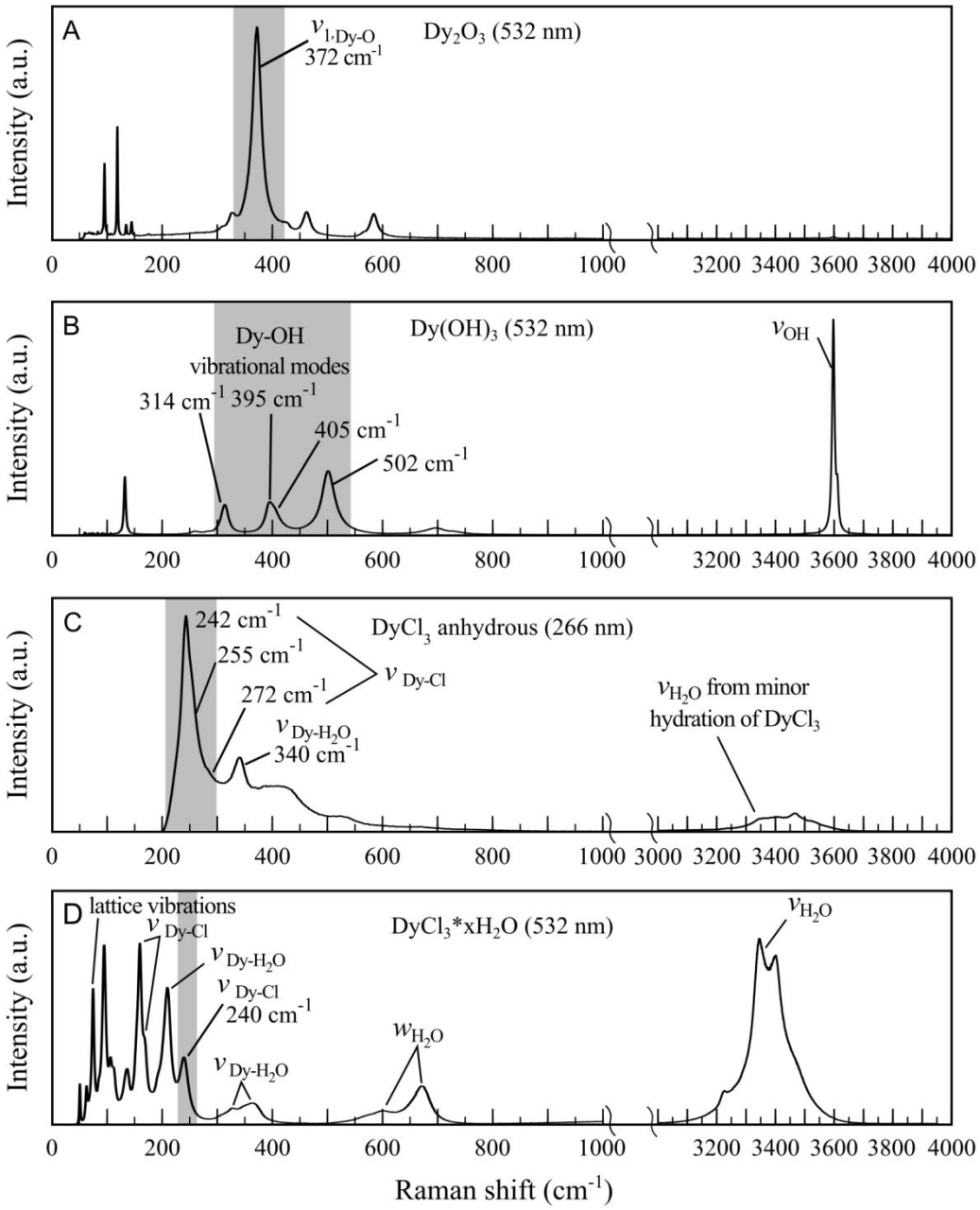

526

527 **Figure 2:** Raman spectra of reference Dy solids. A) Dy-sesquioxide showing one large peak for

528 Dy-O at 372 cm^{-1}. B) Dy-hydroxide showing three peaks for Dy-OH at 314, 395 cm^{-1} with a

529 shoulder at 405, and 502 cm^{-1}. C) Anhydrous Dy chloride showing a dominant peak at 242 cm^{-1}

530 for Dy-Cl bonds. D) Hydrated Dy chloride exhibiting a similar peak at 240 cm^{-1} for Dy-Cl

531 compared to the anhydrous solid.

532

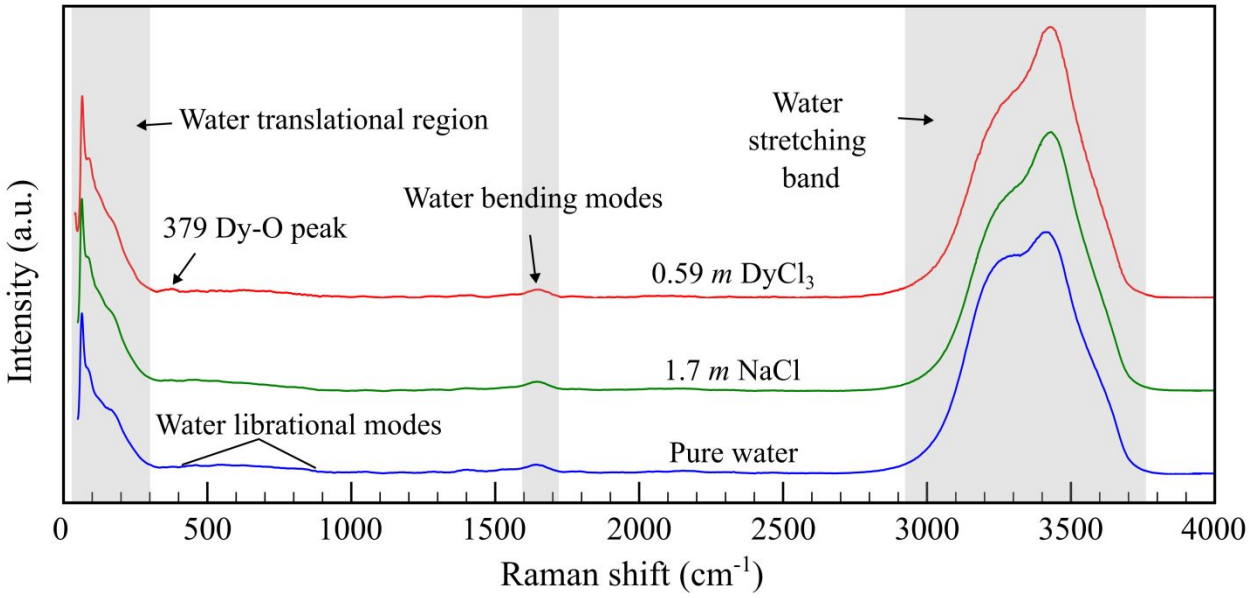

533 **Figure 3:** Raman spectra at ambient temperature for pure water (MilliQ), 1.7 mol/kg NaCl pH 2
534 solution, and 0.59 mol/kg $DyCl_3$ pH 2 solution showing the major features of the water band
535 including translational, librational, bending, and stretching modes and the Dy-O band at 379 cm^{-1}
536 [1].

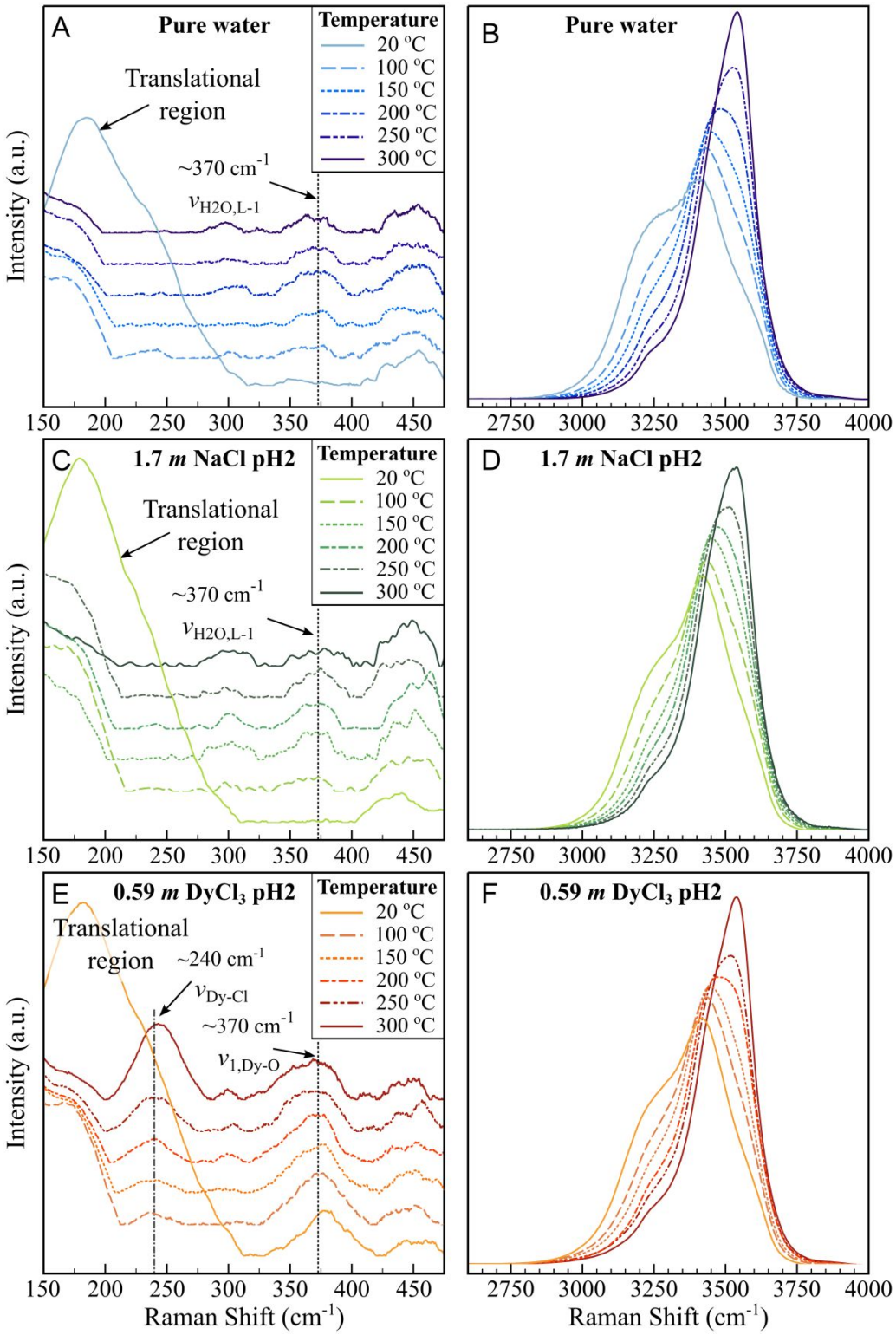
A
Pure water
Translational region
~370 cm-1
νH2O,L-1
Temperature
20 °C
100 °C
150 °C
200 °C
250 °C
300 °C
Intensity (a.u.)
B
Pure water
C
1.7 m NaCl pH2
Translational region
~370 cm-1
νH2O,L-1
D
1.7 m NaCl pH2
E
0.59 m DyCl3 pH2
Translational region
~240 cm-1
νDy-Cl
~370 cm-1
ν1,Dy-O
F
0.59 m DyCl3 pH2
150 200 250 300 350 400 450
2750 3000 3250 3500 3750 4000
Raman Shift (cm-1)

537

538 **Figure 4:** Corrected Raman spectra of the low-frequency region (A, C, E) and stretching
539 vibrations of water (B, D, F) with increasing temperature from 20–300 °C. In the low-frequency
540 region, the translational water modes decrease in peak intensity and shift to lower wavenumbers
541 with increasing temperature in A) pure water, C) NaCl-bearing and E) $DyCl_3$-bearing solutions.
542 Librational modes of water appear at 300 and 370 cm^{-1} with increasing temperature in all
543 solutions, (E) with the mode at 370 cm^{-1} being overprinted by the larger Dy-O mode in $DyCl_3$-
544 bearing solutions. The stretching vibrational band of water systematically shifts to higher
545 wavenumbers with increasing temperature (B, D, F).
546

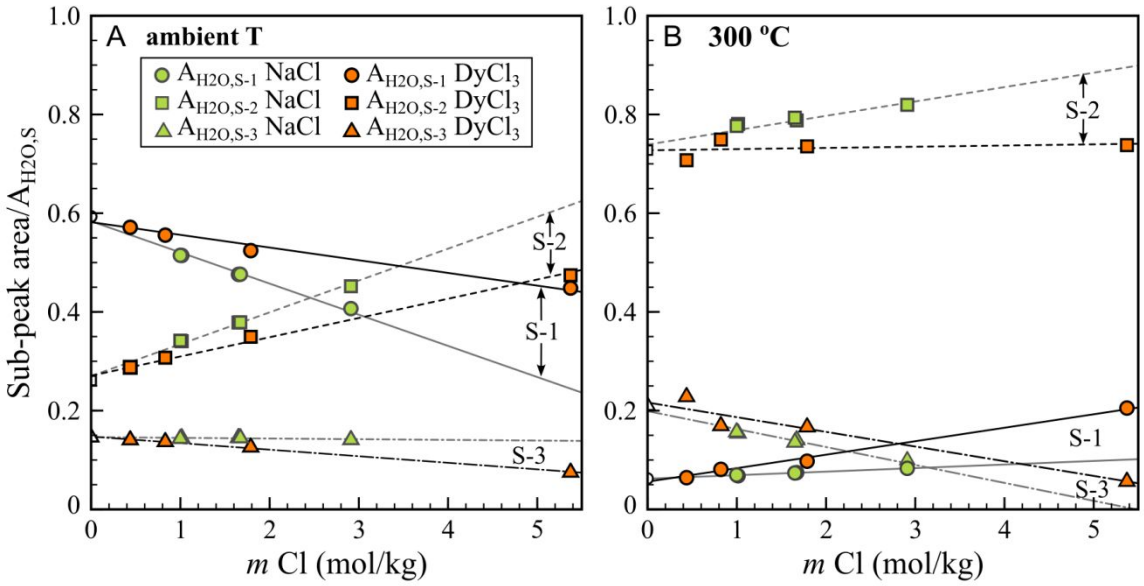

547 **Figure 5:** Systematic trends in the area fraction contributions of the three sub-peaks (S-1 to S-2)
548 to the total water stretching band as a function of Cl concentration in NaCl-bearing and $DyCl_3$-
549 bearing solutions. A) At ambient temperature, in Cl poor solutions sub-peak S-1 dominates the
550 and decreases with increasing Cl content and becomes equal to sub-peak S-2 above ~3 mol/kg
551 Cl. Sub-peak 3 S-3 is the smallest peak and only shows minor variation with increasing Cl
552 content. B) At 300 °C, S-2 is the dominant peak at all Cl concentrations, showing little variation
553 in $DyCl_3$-bearing solutions and increases in NaCl-bearing solutions. S-1 and S-3 comprise minor
554 contributions to the water band, with S-1 increasing and S-3 decreasing with increasing Cl
555 concentrations.
556

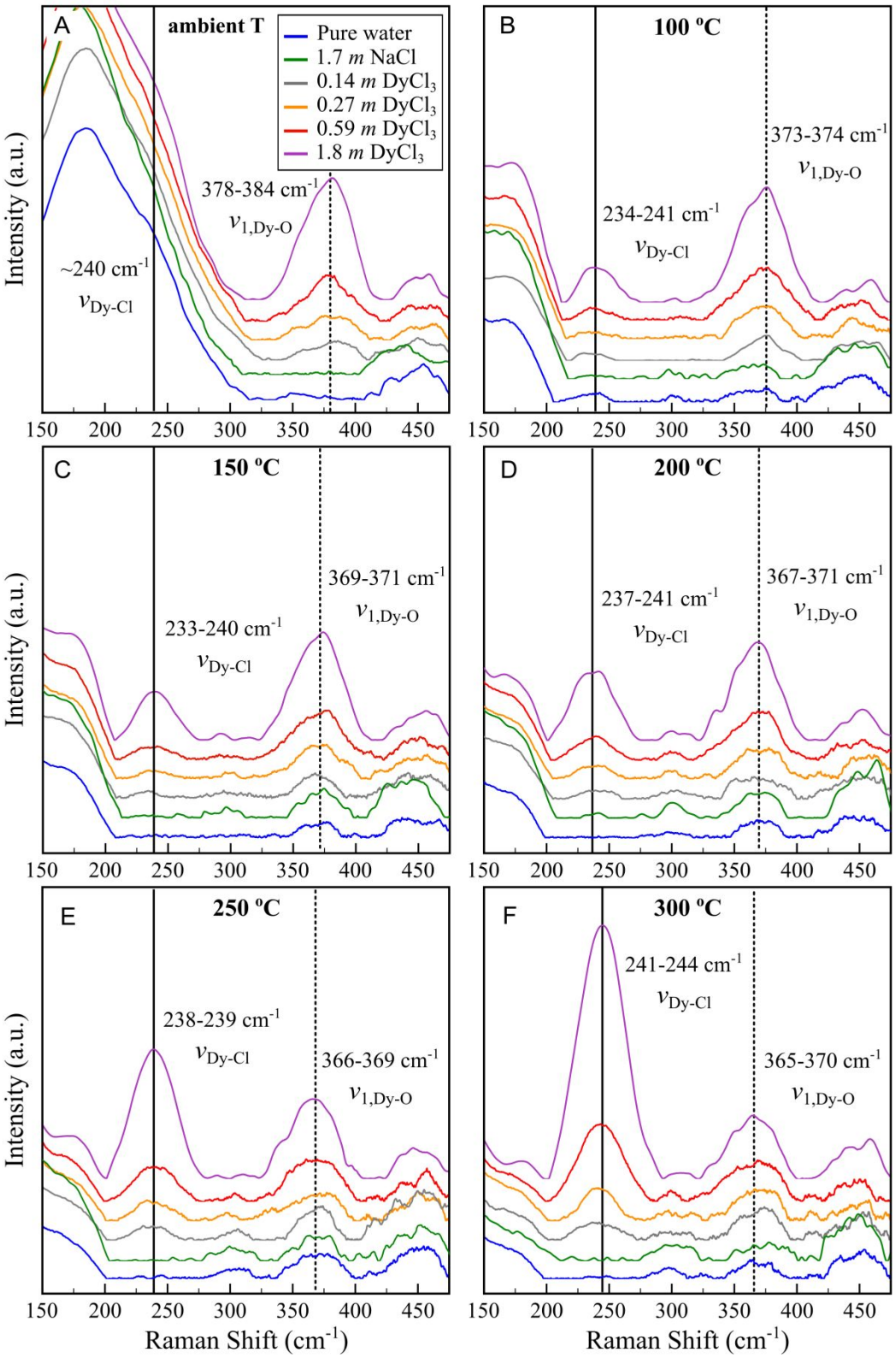

557 **Figure 6:** Raman spectra from 150 to 475 cm^{-1} of pH 2 solutions with increasing dissolved

$DyCl_3$ concentrations, pure water (MilliQ) and the 1.7 mol/kg NaCl background solution at 20–300 °C. A) At ambient temperature the edge of the water translational bands obscures the Dy-Cl vibrational band at 240 cm^{-1}. The Dy-O vibrational band at 378-384 cm^{-1} increases with increasing $DyCl_3$ concentrations. With increasing temperature B) 100 °C, C) 150 °C, D) 200 °C, E) 250 °C, F) 300 °C the Dy-O vibrational band (~370 cm^{-1}) decreases and the Dy-Cl vibrational band (~240 cm^{-1}) increases. The spectra are plotted as reduced intensities and are off-set using a constant value for better visualization.

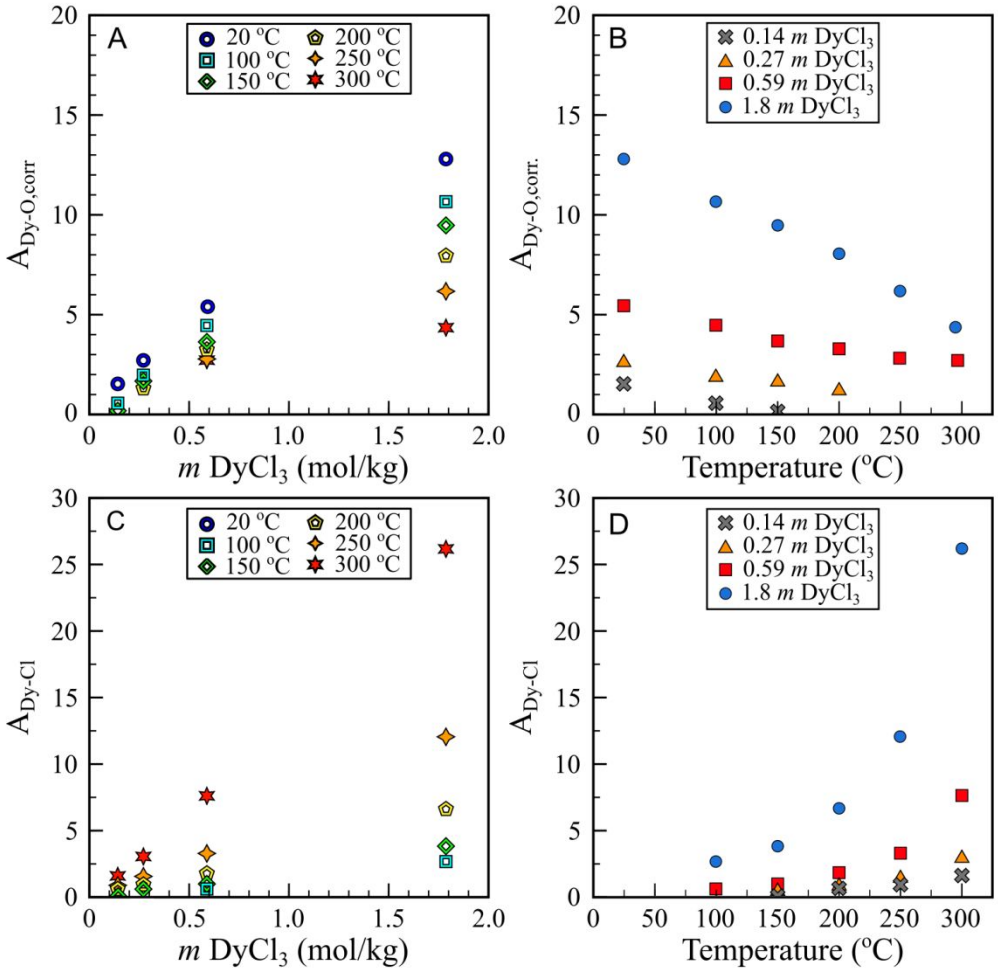

565

566 **Figure 7:** Peak areas for the reduced and normalized Dy-O and Dy-Cl bands as a function of

567 total dissolved $DyCl_3$ and temperature. A) Corrected peak area of the Dy-O band ($A_{Dy\text{-}O,corr.}/A_{H2O}$) for each isotherm as a function of total dissolved $DyCl_3$ in mol/kg and B) as a

569 function of temperature. C) Peak area of the Dy-Cl band ($A_{Dy\text{-}Cl}/A_{H2O}$) for each isotherm as a

570 function of total dissolved $DyCl_3$ and D) as a function of temperature.

571

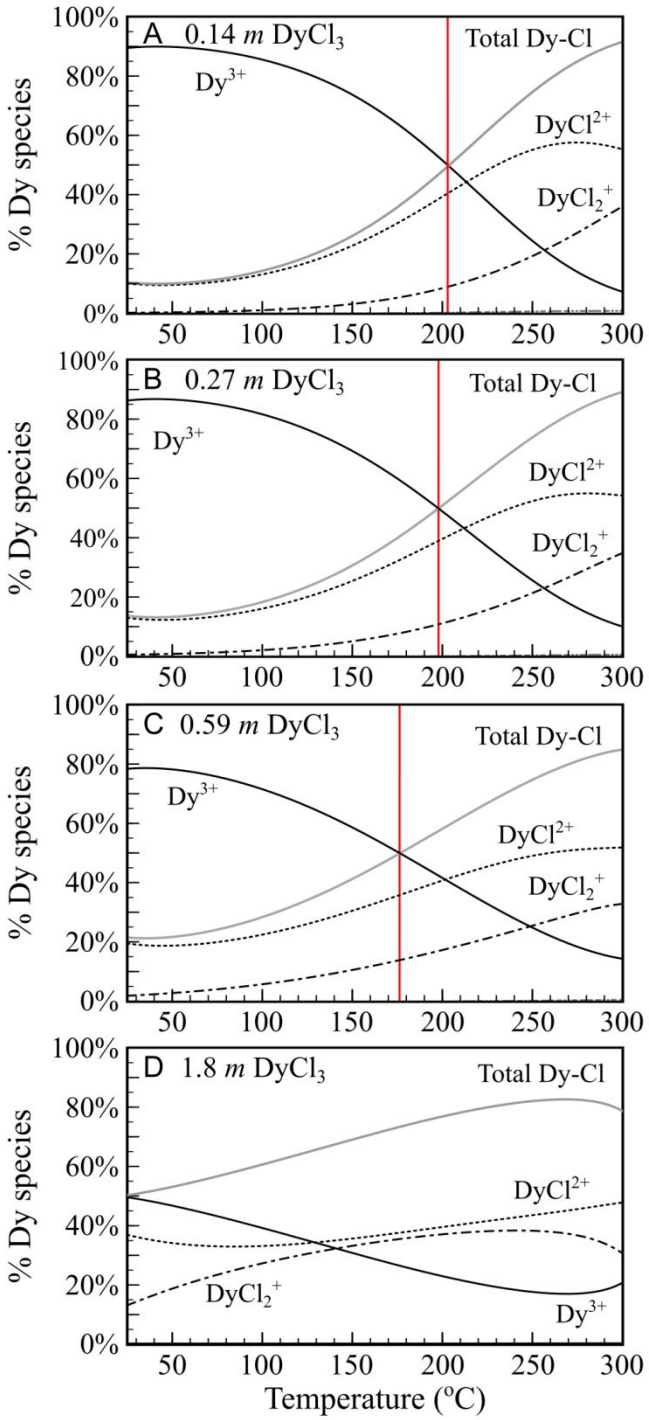

572

573 **Figure 8:** Simulated Dy speciation as a function of temperature. A) The 0.14 mol/kg $DyCl_3$ pH 2

574 experimental solution, B) the 0.27 mol/kg $DyCl_3$, pH 2 experimental solution, C) the 0.59 mol/kg

575 $DyCl_3$ pH 2 experimental solution, and D) the 1.8 mol/kg $DyCl_3$ pH 2 experimental solution. The
576 vertical red lines in A), B), and C) represent the temperatures at which speciation shifts from
577 Dy^{3+} aqua ion dominant to Dy chloride species dominant. Thermodynamic equilibrium
578 calculations were conducted using the GEMS code package and the MINES thermodynamic
579 database. The thermodynamic properties for Dy are from Shock and Helgeson[111] and Shock et
580 al.[80] for Dy^{3+}, from Migdisov et al.[11] for Dy chloride species.
581

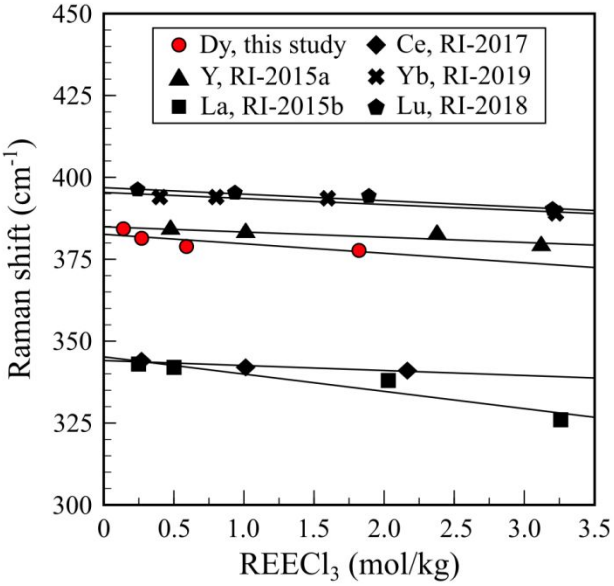

582 **Figure 9:** Peak center positions of the REE-O bond ($\nu_{1,REE-O}$) shift to lower wavenumbers with
583 increasing dissolved $REECl_3$ concentration at ambient temperature. Peak center positions of
584 REE-O bonds shift to higher wavenumbers with decreasing ionic radii of the REE^{3+} aqua ion and
585 the systematic trend with increasing $DyCl_3$ concentrations can be fit to a linear function (solid
586 black lines). References: RI-2015a = Rudolph and Irmer (2015a); RI-2015b = Rudolph and Irmer
587 (2015b); RI-2017 = Rudolph and Irmer (2017); RI-2018 = Rudolph and Irmer (2018); RI =
588 Rudolph and Irmer (2019).
589

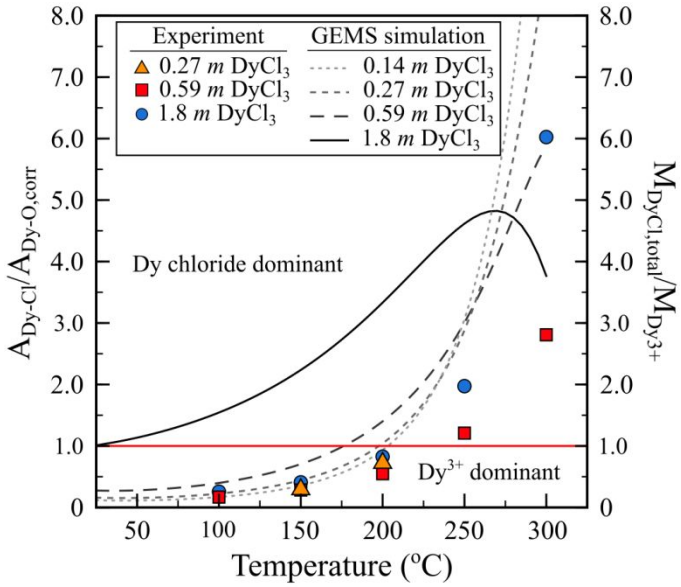

590 **Figure 10:** Comparison of the relative abundance of hydrated Dy^{3+} and Dy chloride species in
591 experimental solutions using the ratio of the peak areas ($A_{Dy\text{-}Cl}/A_{Dy\text{-}O,corr}$) and the simulated mol
592 ratio ($M_{DyCl,total}/M_{Dy3+}$). The red line at $M_{DyCl,total}/M_{Dy3+} = 1$ indicates the boundary between Dy^{3+}
593 dominant and Dy chloride species dominant fields.

594

595

596

597

598

599

Tables:

Table 1: Composition of all experimental solutions.

Solution ID	T °C	pH (25 °C)	HCl mol/L	$DyCl_3$ mol/kg	NaCl mol/kg	Cl mol/kg	Cl/Dy
			Pure water				
MilliQ	20-300	7.00	-	-	-	-	-
			Water-NaCl-HCl				
1 *m* NaCl-pH2	20-300	2.00	0.01001	-	1.00	1.01	-
1.7 *m* NaCl-pH2	20-300	2.02[a]	0.01002	-	1.66	1.67	-
1.7 *m* NaCl-pH4	20-300	3.99[a]	0.00012	-	1.65	1.65	-
1 *m* NaCl-pH5	20-300	5.01	0.00001	-	1.00	1.00	-
3 *m* NaCl-pH7	20-300	6.93[a]	-	-	2.91	2.91	-
			Water-$DyCl_3$-HCl				
0.14 *m* $DyCl_3$-pH2	20-300	2.03	0.01102	0.142	-	0.44	3.08
0.27 *m* $DyCl_3$-pH2	20-300	2.01	0.01032	0.271	-	0.82	3.04
0.59 *m* $DyCl_3$-pH2	20-300	2.17[a]	0.00995	0.593	-	1.79	3.02
1.8 *m* $DyCl_3$-pH2	20-300	2.27[a]	0.01102	1.788	-	5.37	3.01

[a] pH calculated using GEM-Selektor from pH measured in dilute salt free HCl solutions and added salt amount.

Table 2: Raman modes of the main vibrational peak centers for Dy-O and Dy-Cl in reference Dy solids measured using the 532 nm and the 266 nm excitation laser.

Raman modes	Dy_2O_3 cm^{-1}	Dy_2O_3 cm^{-1}	$Dy(OH)_3$ cm^{-1}	$Dy(OH)_3$ cm^{-1}	$DyCl_3$ cm^{-1}	$DyCl_3 \cdot xH_2O$ cm^{-1}	$DyCl_3 \cdot xH_2O$ cm^{-1}
Laser (nm)	532	266	532	266	266	532	266
$\nu_{s,\ Dy\text{-}Cl}$[a]						153-159	
$\nu_{as,\ Dy\text{-}Cl}$[a]						240	237-269
$\nu_{Dy\text{-}Cl}$[b]					242-272		
$\nu_{Dy\text{-}O}$[c-e]			314-502	311-499			
$\nu_{1,Dy\text{-}O}$[e-g]	372	370					
$\nu_{1,Dy\text{-}H2O}$[a]						315-359	314-348
$\nu_{,H2O}$[a]						3224-3442	3231-3444
ν_{OH}[c-e]			3597-3611	3598-3612			

References: (a) Oczko and Macalik [90]; (b) Papatheodorou [87]; (c) Arunachalam et al. [115]; (d) Sanivarapu et al. [85]; (e) Hurtig et al. [80]; (f) Schaack and Koningstein [81] ; (g) Abrashev et al. [75].

611 Table 3: Peak center positions and peak areas in the range of 300-400 cm^{-1} and total area of

612 water stretching band ($A_{H2O,S}$) for background solutions.

Solution ID	T	$\nu_{H2O,L-1}$	$A_{H2O,L-1}$	$\nu_{H2O,S}$	$A_{H2O,S}$
	°C	cm^{-1}		cm^{-1}	
MilliQ	20	-	-	3271-3588	98909
MilliQ	100	367.3	1.197	3288-3584	98916
MilliQ	150	370.5	1.077	3323-3578	98516
MilliQ	200	370.8	1.263	3291-3579	98702
MilliQ	250	370.2	2.360	3247-3571	98303
MilliQ	300	367.6	1.264	3251-3566	98781
1 *m* NaCl-pH2	20	-	-	3271-3588	99268
1 *m* NaCl-pH2	100	372.4	1.237	3288-3584	98795
1 *m* NaCl-pH2	150	369.7	1.318	3323-3578	98288
1 *m* NaCl-pH2	200	371.5	1.261	3291-3579	98764
1 *m* NaCl-pH2	250	372.7	1.552	3247-3571	99107
1 *m* NaCl-pH2	300	367.1	1.575	3251-3566	97645
1.7 *m* NaCl-pH2	20	-	-	3271-3588	99235
1.7 *m* NaCl-pH2	100	367.0	1.236	3288-3584	98658
1.7 *m* NaCl-pH2	150	367.4	1.610	3323-3578	98948
1.7 *m* NaCl-pH2	200	369.9	1.880	3291-3579	98386
1.7 *m* NaCl-pH2	250	369.3	2.031	3247-3571	98749
1.7 *m* NaCl-pH2	300	376.2	1.920	3251-3566	98417
1.7 *m* NaCl-pH4	20	-	-	3271-3588	99201
1.7 *m* NaCl-pH4	100	369.5	1.224	3288-3584	98928
1.7 *m* NaCl-pH4	150	370.2	1.738	3323-3578	98818
1.7 *m* NaCl-pH4	200	367.9	1.942	3291-3579	98764
1.7 *m* NaCl-pH4	250	367.3	2.110	3247-3571	98901
1.7 *m* NaCl-pH4	300	368.1	2.442	3251-3566	98149
1 *m* NaCl-pH5	20	-	-	3271-3588	99266
1 *m* NaCl-pH5	100	372.9	1.162	3288-3584	98751
1 *m* NaCl-pH5	150	369.8	1.185	3323-3578	98740
1 *m* NaCl-pH5	200	370.1	1.347	3291-3579	98751
1 *m* NaCl-pH5	250	374.6	1.654	3247-3571	98936
1 *m* NaCl-pH5	300	365.3	1.692	3251-3566	98399
3 *m* NaCl-pH7	20	-	-	3271-3588	99140
3 *m* NaCl-pH7	100	374.3	1.252	3288-3584	98933
3 *m* NaCl-pH7	150	370.6	1.944	3323-3578	98993
3 *m* NaCl-pH7	200	370.7	2.263	3291-3579	98830
3 *m* NaCl-pH7	250	368.8	1.645	3247-3571	98781
3 *m* NaCl-pH7	300	370.0	1.962	3251-3566	97884

613

614 Symbols: $\nu_{H2O,L-1}$ = peak center position of the librational mode in background solutions used to

615 correct $\nu_{1,Dy\text{-}O}$; ν_{H2O} range of peak centers for the water stretching band at 300-3800 cm^{-1}; $A_{H2O,L\text{-}1}$

616 = peak area of the librational mode in background solutions used to correct $\nu_{1,Dy\text{-}O}$; $A_{H2O,S}$ = total

617 peak area of the water stretching band.

Table 4: Peak center positions and peak areas for Dy-O and Dy-Cl Raman modes in the range of 200-400 cm^{-1} in $DyCl_3$-bearing solutions.

		Dy-O		*Dy-Cl*				
Solution ID	T	$\nu_{1,\ Dy\text{-}O}$	$A_{Dy\text{-}O,corr}$	$\nu_{Dy\text{-}Cl}$	$A_{Dy\text{-}Cl}$	$A_{Dy\text{-}Cl}/A_{Dy\text{-}O,corr}$	$\nu_{H2O,S}$	$A_{H2O,S}$
	°C	cm^{-1}		cm^{-1}			cm^{-1}	
0.14 *m* $DyCl_3$-pH2	20	384.3	1.533	-	-	-	3271-3588	99347
0.14 *m* $DyCl_3$-pH2	100	374.0	0.5677	-	-	-	3288-3584	98827
0.14 *m* $DyCl_3$-pH2	150	368.7	0.1865	*233.2*	*0.3173*	*1.702*	3323-3578	98556
0.14 *m* $DyCl_3$-pH2	200	-	-	240.7	0.6008	-	3291-3579	98601
0.14 *m* $DyCl_3$-pH2	250	-	-	237.7	0.9141	-	3247-3571	98202
0.14 *m* $DyCl_3$-pH2	300	-	-	241.0	1.589	-	3251-3566	97047
0.27 *m* $DyCl_3$-pH2	20	381.4	2.711	-	-	-	3271-3588	99215
0.27 *m* $DyCl_3$-pH2	100	372.8	1.970	-	-	-	3288-3584	98754
0.27 *m* $DyCl_3$-pH2	150	370.7	1.734	239.5	0.4825	0.2782	3323-3578	98633
0.27 *m* $DyCl_3$-pH2	200	370.3	1.299	238.5	0.9373	0.7215	3291-3579	98538
0.27 *m* $DyCl_3$-pH2	250	-	-	238.5	1.559	-	3247-3571	98250
0.27 *m* $DyCl_3$-pH2	300	-	-	242.1	3.047	-	3251-3566	97586
0.59 *m* $DyCl_3$-pH2	20	378.6	5.399	-	-	-	3271-3588	99085
0.59 *m* $DyCl_3$-pH2	100	373.3	4.422	239.0	0.6268	0.1417	3288-3584	98725
0.59 *m* $DyCl_3$-pH2	150	370.6	3.635	238.4	1.000	0.2751	3323-3578	98672
0.59 *m* $DyCl_3$-pH2	200	367.6	3.242	238.1	1.780	0.5490	3291-3579	98611
0.59 *m* $DyCl_3$-pH2	250	367.6	2.773	239.0	3.283	1.184	3247-3571	98445
0.59 *m* $DyCl_3$-pH2	300	365.5	2.707	243.7	7.601	2.808	3251-3566	97574
1.8 *m* $DyCl_3$-pH2	20	378.0	12.80	-	-	-	3271-3588	98219
1.8 *m* $DyCl_3$-pH2	100	372.7	10.66	240.8	2.683	0.2516	3288-3584	98553
1.8 *m* $DyCl_3$-pH2	150	370.3	9.473	240.4	3.838	0.4052	3323-3578	98836
1.8 *m* $DyCl_3$-pH2	200	367.1	8.006	237.0	6.612	0.8258	3291-3579	98567
1.8 *m* $DyCl_3$-pH2	250	366.1	6.164	239.3	12.05	1.954	3247-3571	99499
1.8 *m* $DyCl_3$-pH2	300	365.3	4.342	244.5	26.16	6.025	3251-3566	97940

Symbols: $\nu_{1,Dy\text{-}O}$ = peak center position of the main stretching vibration of the Dy-O bond; $\nu_{Dy\text{-}Cl}$ = peak center position of the main stretching vibration of the Dy-Cl bond; ν_{H2O} range of peak centers for the water stretching band at 3000-3800 cm^{-1}; $A_{Dy\text{-}O}$ = peak area of the Dy-O mode; $A_{Dy\text{-}Cl}$ = peak area of the Dy-Cl mode; $A_{H2O,S}$ = total peak area of the water stretching band. Italic notation: high uncertainty, excluded from evaluation of speciation.

The data supporting this article have been included as part of the Electronic Supplementary Information (ESI).